Federal University of Ceara

Department of Physics

ZHANG NANA

Growth and Vibrational Properties of Oxide Crystals

Fortaleza/CE

2012

ZHANG NANA

Growth and Vibrational Properties of Oxide Crystals

Advisor: Prof. Dr. Ilde Guedes da Silva

A dissertation submitted to the Department of Physics of the Federal University of Ceara in partial fulfillment of the requirements for the Degree of Doctor of Physics.

Fortaleza/CE

2012

Dados Internacionais de Catalogação na Publicação
Universidade Federal do Ceará
Bibioteca do Curso de Física

Z61g Zhang, Nana

Growth and Vibrational Properties of Oxide Crystals / Nana zhang. - Fortaleza, 2012.
104 f.: il. color., enc.; 30cm.

Tese (Doutorado) - Universidade Federal do Ceará, Centro de Ciências, Departamento de Física, Fortaleza, 2012.
Área de concentração: Física da Matéria Condensada.
Orientador: Prof. Dr. Ilde Guedes da Silva.

1. Raman Spectroscopy. 2. Thermal Propeties. 3. Crystals. 4. Phase Transition I. Título.

CDD 535.846

Nana Zhang

Crescimento e propriedades vibracionais de cristais a base de óxidos

Tese submetida à Coordenação do Curso de Pós-Graduação em Física, da Universidade Federal do Ceará, como requisito parcial para a obtenção do grau de Doutor em Física.

Aprovada em 16 / 03 / 2012

BANCA EXAMINADORA

Dr. Ilde Guedes da Silva - Orientador
UFC

Dr. Paulo Sergio Pizani
UFSCAR

Dr. Samuel Leite Oliveira
UFMS

Dr. Josué Mendes Filho
UFC

Dr. Alejandro Pedro Ayala
UFC

ACKNOWLEDGMENTS

► I would like to express my deep and sincere gratitude to my advisor, Dr. Ilde Guedes da Silva, who provided me all the support for the realization of the Raman scattering experiments, his wide knowledge and enthusiastic way of working have been of great value to me. All these qualities will be good for my future career. It was my honor and it has been really rewarding to work with him. Here, it was also my great pleasure to know his family.

► I owe my deep gratitude to my advisor Prof. Jiyang Wang (China) whose collaboration with the Raman Group of the Department of Physics of the Federal University of Ceara, turns out possible my stay in Brazil. Under his guidance I became more courageous and mature.

► I wish to express my warm and sincere thanks to Prof. Dr. Alejandro Pedro Ayala, who always helped and encouraged me, and for the enlightening discussions on my work.

► I would like to express my deep thanks to Prof. Dr. Antônio Gomes Souza Filho and Prof. Dr. Eduardo Bêde Barros, for critical reading this work and participate of my qualifying.

► I would like to express my deep gratitude to the other members of my Examination Committee for my doctoral dissertation, Prof. Dr. Josué Mendes Filho, Prof. Dr. Paulo Sérgio Pizani and Prof. Dr. Samuel Leite Oliveira, for the critical readings.

► I would like to show my gratitude to the staffs in the secretary and the others professors of the Department of Physics of UFC, for their kind help and encouragements.

► I would like to express my deep gratitude to my roommate and great friend Sara. We spent two years together, and I am honored to have her friendship.

► I would like express the deep gratitude to my Jiejie Mylene and all her family (my family in Brazil). When I encountered difficulties, they were always by my side, no words can describe my grateful for them, and I wish all their life becomes happier and happier.

► I am grateful for my good friend Clenílton, for his selfless help on the professional knowledge and for his always words of encouragement “don´t worry”.

► I express appreciation to my friend Leandro, who is interested in Chinese culture. We helped each other in learning the languages; thanks for his encouragements.

► I would like to show my gratitude to my friend Vagner, who gave me great help on my normal student life whenever I asked for.

► I express my gratitude to all the friends I knew in Brazil, namely: Gadelha, Otavio, Manuela, Glaydson, Diego, *et al*. Many thanks for all of their kind help.

► I can not forget to thank Profs. Alice and Glaucya, with their great encouragements, I could pass the language exams.

► One word, I would like to express my appreciation to any person I knew here, all of them were so kind to me, it was my great pleasure to spend two years in this beautiful and happy country--BRAZIL.

► I would like to thank the Department of Physics of the Federal University of Ceara and the State Key Laboratory of Crystal Materials of Shandong University.

► Finally, financial support from the Brazilian agency CNPq and China Scholarship Council are acknowledged.

SPECIAL ACKNOWLEDGMENTS

To my parents that during so many years have supported, encouraged and taught me. Their selfless love is my greatest power forward.

To my parents in-law, whose understanding and support have increased my confidence to come and study in Brazil.

To my dear brother and his wife. You took good care of our parents, and our beloved family provided me good conditions to finish my learning.

To my husband Liu Peng. Thank you for the support, thank you for my tolerance, thank you for your endless love…. You gave me hugs, filled my life with happiness, gave me wings, and filled my life with dreams. Due to you I could touch the sky….We made it!.

"*Do or do not…There is no try.*"

(Yoda-Star Wars)

ABSTRACT

In this work we used different experimental techniques to study four different series of inorganic oxide crystals, namely: (i) congruent lithium isotope niobate (C^7LN), (ii) rare-earth doped mixed vanadates ((Nd,Yb):$Y_xGd_{1-x}(VO_4)$); (iii) alkali metal doped and pure calcium barium niobates ($Ca_xBa_{1-x}Nb_2O_6$); and (iv) potassium tantalite niobate ($KTa_{1-x}Nb_xO_3$). Below we describe the studies performed for each class.

(i) For further investigation on the defect structure of lithium niobate crystals ($LiNbO_3$ – hereafter LN) using the neutron scattering technique, a congruent lithium isotope niobate crystal (C^7LN) was grown by the Czochralski method from a 48.4% ^7Li melt. The X-ray powder diffraction (XRPD) results show that the as-grown crystal is a single-phased ($R3c$) LN. We observed $4A_1(TO)+7E(TO)$ Raman modes. The crystal composition (Li mol%) determined from UV absorption edge and Raman measurements is 47.47% and 47.34%, respectively. The specific heat (C_p), thermal diffusion coefficients (λ_a , λ_c), thermal conductivities (κ_a , κ_c) and the average thermal expansion coefficients (α_a , α_c) were determined. The effect of Li vacancy content is analyzed by comparing the results with those obtained for near stoichiometric lithium isotope niobate (NS^7LN) and congruent natural lithium niobate (CLN) crystals. The values of all thermal parameters of C^7LN are smaller than those of NS^7LN and CLN, which may be related to either the difference of vacancy content or isotope substitution.

(ii) The room temperature phonon modes of the isostructural (Nd,Yb):$Y_xGd_{1-x}(VO_4)$ laser crystals were determined using the Raman scattering technique, and the observed wavenumbers follow the overall mode distribution expected for $REVO_4$ (RE = rare earth)

compounds with the tetragonal zircon structure, D_{4h}^{19}. They were assigned according to the group theory in terms of the internal modes of the VO_4 tetrahedron and the external modes of the $Y_xGd_{1-x}(VO_4)$ lattice. No appreciable changes in the phonon wavenumbers were observed for Yb:$GdVO_4$ (Yb = 0.008, 0.015, 0.020, 0.025, and 0.035), indicating that the force fields in the $GdVO_4$ lattice are not strongly altered by Yb doping at the Gd site. However, most of the phonon wavenumbers in the systems (Nd,Yb):$Y_xGd_{1-x}(VO_4)$ shifts upwards (one-phonon-like behavior) when Y replaces Gd.

(iii) The room temperature phonon modes of both the alkali metal doped and pure $Ca_xBa_{1-x}Nb_2O_6$ (hereafter CBN_x) crystals were determined using the Raman scattering technique. Owing to the intrinsic disorder of the tetragonal lattice we observed few and broad bands. The wavenumber of the internal modes observed shifts upwards when the volume of the unit cell increases. This blue shift is likely to be related to the shortening of the Nb-O band length of the NbO_6 octahedrons. The Curie temperatures of the ferroelectric to paraelectric phase transition for all the CBN-like crystals were obtained from DSC measurements. The Raman spectra of CBN32 in the temperature range from 300 to 568 K were recorded in order to investigate and verify the ferroelectric phase transformation. The lower-temperature (25-260 K) dependent Raman spectra of CBN32 were also recorded, and the results show that it may exhibit a phase transition at 75-100 K.

(iv) Single crystals of potassium tantalite niobate, $KTa_{1-x}Nb_xO_3$ (KTN_x, x = 0.45, 0.50, and 0.55), were synthesized by the top-seeded solution growth method. The Raman scattering technique is used to investigate the sequence of phase transitions undergone by KTN_x crystals. Special attention is given to the changes which characterize the orthorhombic-to-rhombohedral phase transition.

CONTENTS

LIST OF FIGURES

LIST OF TABLES

1

INTRODUCTION

Here we present a review of the main results already published for each class of oxide crystals considered and describe the main goals of this work.

1.1 Isotope lithium niobate ($^{7}LiNbO_3$) crystal

Lithium niobate ($LiNbO_3$, hereafter LN) crystal is an important multi-functional crystal, which posses good piezo-electric, nonlinear-optic, electro-optic and photorefractive properties, which has been widely used for tailoring optical and piezoelectric devices [1-3].

Congruent lithium niobate (CLN) crystals, which can be readily grown from a melt composition with 48.4% Li_2O and 51.6% Nb_2O_5 by Czochralski method [4]， however, due to the fact CLN is a non-stoichiometric compound with a compositional range of approximately 47-50 mol% Li_2O [5], the intrinsic defects associated with the stoichiometry influence seriously the properties of this material. Therefore, it is necessary to further investigate the micro-structure of LN crystals, and try to research some relationship between the micro-structure and physical properties.

To explain the defect structure, some models based on the cation substitution have been presented. Peterson *et al.* [6] based on the nuclear magnetic resonance measurements (NMR), proposed a Nb vacancy (V_{Nb}) model ($[Li_{1-x}Nb_x]\ [Nb_{1-4x/5}(V_{Nb})_{4x/5}]O_3$), which was later supported by the single crystal X-ray diffraction measurements performed by Abrahams *et al.* [7]. Lerner *et al.* [8] proposed a Li vacancy (V_{Li}) model ($[Li_{1-x}Nb_{x/5}(V_{Li})_{4x/5}]\ NbO_3$),

which was supported by the X-ray and neutron diffraction [9-11], NMR [12] and Raman scattering results [13]. Although several efforts have been made to understand its intrinsic lattice characteristics, there still remains a controversy on the defect structure of LN.

The X-ray diffraction technique is a common and important tool to resolve crystal structure. However, due to the fact that the X-ray scattering technique is mainly related with the electron clouds, the scattering length is proportional to the atomic number what makes it unsensitive to light atoms. On the other hand, since the neutron scattering technique is related to the atomic nucleus, it may be used to determine the specific positions of light atoms. For LN crystal, consisting of O, Li, and H light elements, the nuclear scattering lengths of Li (-1.900 fm) and Nb (7.054 fm) are of the same order but have opposite sign, indicating that the neutron diffraction technique is a powerful tool to reveal the LN crystal structure.

The natural Li element contains two isotopes: ^{6}Li and ^{7}Li. The good quality single crystal grown with natural Li (7.4% of ^{6}Li) is not suitable for neutron scattering measurements, because the ^{6}Li isotope has a large neutron absorption cross section (940 barn) as compared with ^{7}Li (0.0454 barn) isotope, and both isotopes are randomly distributed in the crystal lattice. To neutron diffraction experiments, the existence of ^{6}Li isotope can absorb part of neutrons from the neutron source. Therefore, the search for growing single crystal from separated ^{7}Li isotope is advisable.

To date, we found the following investigations about the isotope LN materials, Repelin *et al.* [14] used polarized Raman spectroscopy to investigate the optical phonons of ^{7}LN and ^{6}LN polycrystalline samples. Martin *et al.*[15] used the NMR technique to investigate the lithium diffusion in the ^{7}LN amorphous compound. Chowdhury *et al.* [16, 17] reported on the lattice dynamics of the ^{7}LN single crystal using neutron inelastic scattering technique. However, some of the physical properties as well as the Raman and infrared phonons of the ^{7}Li-enriched $LiNbO_3$ crystal are still not well understood.

Therefore, in Chapter 2 we will report on the detailed growth of C^7LN single crystal and the characterizations of its primary properties.

1.2 Mixed-vanadate ((Nd,Yb):$Y_xGd_{1-x}(VO_4)$) crystal

The laser diode pump solid-state lasers (DPSSL) present high pumping efficiency and stable output power. DPSSL have found many important applications in different areas such as: material processing, medicine, optical communications, laser displays and laser nuclear fusion. Owing to these facts the search for laser materials that can be used as active media for DPSSL lasers is very important.

Neodymium-doped yttrium vanadate (Nd:YVO_4) crystal is likely one of the most investigated laser crystals so far. It possesses excellent mechanical, physical, chemical, and lasing properties. In the lamp pump era, researchers did not pay much attention to Nd:YVO_4 crystal owing to its low thermal conductivity, and the YAG crystal takes the main role as laser host medium. However, with the development of high power light emitting diodes (LED) in the 1980´s the excellent laser properties of Nd:YVO_4 crystal have been noticed. Nowadays, the highest output power at fundamental wavelength is of the order of 35 W [18], and the output power of intro-cavity doubled green laser is about 20 W [19].

Neodymium-doped gadolinium vanadate Nd:$GdVO_4$ crystal was first reported in 1992 [20]. The laser properties of Nd:$GdVO_4$ crystal may be better than those of Nd:YVO_4, since the former possesses high thermal conductivity [21].

A large number of papers demonstrating laser action in the systems Nd:YVO_4 and Nd:$GdVO_4$ have already been published [22-30]. Since they are isostructural and have similar melting points, it is possible to obtain an infinite soluble Nd:$Y_xGd_{1-x}VO_4$ solution and grow crystals with good optical quality. Recalling that due to the mixing, the absorption band of the

Nd^{3+} ions can broaden. This broadening has attracted an increasing interest because of its potential application for high pump power pulsed lasers.

Many reports on the laser action of Nd:$Y_xGd_{1-x}VO_4$ crystals in either continuous-wave (cw) or pulsed mode have been demonstrated. In 2010, Liu *et al.* [31] reported on the actively Q-switched laser performance of the Nd:$Y_xGd_{1-x}VO_4$ crystals. Liu *et al*. [32] also reported on the cw laser performance of the $Yb_{0.009}$:$Y_{0.575}Gd_{0.416}VO_4$ crystal. Ng *et al.* [33] demonstrated a passively Q-switched Nd:$Gd_{0.64}Y_{0.36}VO_4$ laser with a Cr^{4+}:YAG saturable absorber. He *et al.* [34] demonstrated a passively mode-locked Nd:$Gd_{0.5}Y_{0.5}VO_4$ laser with a semiconductor saturable absorber mirror. Liu *et al.* [35] discussed the improvement of passive Q-switching performance of Nd:$Gd_{0.64}Y_{0.36}VO_4$ as compared to that of Nd:YVO_4 and Nd:$GdVO_4$. Zhang *et al.* [27] demonstrated laser performance at 1.34 μm for Nd:$Gd_{0.8}La_{0.2}VO_4$. Yu *et al.* [36] demonstrated cw laser performance at 1.06 μm for Nd:$Lu_xGd_{1-x}VO_4$ pumped by a diode laser. However, the vibrational properties of these materials have not been done.

The $REVO_4$ series of compositions (RE = Pr to Lu including Sc and Y) exhibit the tetragonal (zircon-type) D_{4h}^{19} structure with four molecules per unit cell (Z = 4). Because of the tightly bound VO_4 tetrahedral in $REVO_4$, a simplified structure can be considered as being composed of two sublattices of RE and VO_4 "molecules", with both RE and VO_4 occupying the crystallographic sites D_{2d}. For a $REVO_4$ crystal with zircon-type structure, the first-order Raman phonon spectrum consists of narrow lines that correspond to Raman-allowed zone-center modes, which obey definite polarization selection rules.

Room-temperature Raman phonons of some of the $REVO_4$ compounds have been reported previously. Polarized results can be found for $PrVO_4$ [37], $NdVO_4$ [37], $GdVO_4$ [38], $TbVO_4$ [38], $DyVO_4$ [38], and $ErVO_4$ [39], while unpolarized results can be found for $TmVO_4$ [40], $LaVO_4$ [41], $CeVO_4$ [42], $SmVO_4$ [43], $EuVO_4$ [40], $HoVO_4$ [44], $YbVO_4$ [40],

and $LuVO_4$ [44]. Recently, Santos *et al.* [45] provided a more accurate description of the room-temperature phonons for $SmVO_4$, $HoVO_4$, $YbVO_4$, and $LuVO_4$ single crystals. Of the 12 zone-center Raman phonons expected, they observed 10 phonons for $SmVO_4$ and $HoVO_4$ and 9 for $YbVO_4$ and $LuVO_4$. The phonon symmetry assignment was given based on correlations with previous results for other $REVO_4$ compounds. Also, they analyzed the correlation among the observed Raman wavenumbers and the rare earth atomic number (*Z*) in order to determine the extent of the variation as RE increases in *Z* along the lanthanide series.

For a mixed $RE'_xRE''_{1-x}(VO_4)$ crystal the following features may be observed from the phonon spectrum: (i) a broadening of the first-order Raman lines; (ii) activation of forbidden Raman phonons; (iii) appearance of broad Raman bands reflecting the phonon density of states; (iv) wavenumber shifting of some peaks proportional to the concentration of the dopant element (i.e., one-phonon-like behavior), and (v) splitting of some peaks involving different elements that share the same lattice site (i.e., two-phonon-like behavior).

Therefore, in Chapter 3, we will use the Raman spectroscopy to investigate the extent of the modification of the $GdVO_4$ phonons due to the doping of the Gd site by Y, Yb, and Nd.

1.3 Calcium barium niobate (CBN) crystals

Many niobate crystals with the tetragonal tungsten bronze (TTB) structure exhibit excellent piezoelectric, electro-optical and nonlinear optical properties. Among these crystals, $Sr_xBa_{1-x}Nb_2O_6$ (SBN) has been widely investigated. But their applications at high temperature have been limited because of the relatively low phase transition temperature (in the range of 25 to 120 °C, depending on the composition).

The calcium barium niobate ($Ca_xBa_{1-x}Nb_2O_6$, hereafter CBNx) crystal also exhibits a TTB structure. In 2002, Esser *et al*. [46] reported on the growth of the first large CBN single

crystal ($Ca_{0.28}Ba_{0.62}Nb_2O_6$, CBN28) by the Czochralski method. It is found that the Curie temperature (T_C) of CBN28 is 260 °C, much higher than SBN crystal (close to 200 °C), which implies that CBN crystal may be applied more potentially over the high temperature range than SBN crystals.

The TTB structure belongs to the *P*4*bm*(C_{4v}^2) space group with five molecules per unit cell (Z = 5) [47]. The lattice cell formula is $(A_1)_2(A_2)_4(B_1)_2(B_2)_8O_{30}$, where different cations occupy both the A_1 and A_2 symmetry sites, forming a partially filled TTB structure. For SBN [48] and $Pb_{0.6}Ba_{0.4}Nb_2O_6$ (PBN) [49] crystals, the Sr^{2+} cations occupy partially the A_1 symmetry sites, while the Sr^{2+} and Ba^{2+} cations fulfill the A_2 symmetry sites. However, for CBN crystals [47, 50, 51], the Ca^{2+} cations occupy the $A_1(C_4)$ sites, while the Ba^{2+} cations occupy the $A_2(C_s)$ sites. The $B_1(C_{2v})$ and $B_2(C_1)$ symmetry sites are completely filled by Nb atoms, then the theoretically predicted reduced existence region for CBN is $0.2 \leq x \leq 0.4$. Since there are only five Ba^{2+} and Ca^{2+} cations available for six A sites in the unit cell, there is a vacancy distributed among the A sites. Thus, the crystal quality and other proprieties can be improved by means of ions dopant or further molecular design. Therefore, in our group we grew series of CBN crystals included the pure CBN26 and CBN32 crystals as well as the alkali metal doped KNCBN ($K_{0.12}Na_{0.08}Ca_{0.28}Ba_{0.62}Nb_2O_6$) and NCBN ($Na_{0.048}Ca_{0.26}Ba_{0.716}Nb_2O_6$).

To date, there are several studies performed in the CBN crystals. The optical properties of CBN28 were reported by Esser *et al*. [47] in 2003. The thermal and electric properties of CBN28 were reported by Song *et al.* in 2006 [52]. In 2007, Burianek *et al*. [53] reported on the growth of five different CBN compositions in the range $0.22 \leq x \leq 0.35$ and observed that the lattice parameter c_0 changes with varying the Ca content. In 2008, Muehlberg *et al*. [54] investigated how T_C changes in the system $Ca_xSr_yBa_{1-x-y}Nb_2O_6$. Recently, Gao *et al*. [50, 51, 55] investigated the thermal, ferroelectric, and vibrational

properties of Nd:CBN, and the electromechanical and electro-optical properties of CSBN [56]. In Ref. [57], Gao *et al.* used Raman spectroscopy to determine the negative thermal expansion (NTE) changes in the system $((Ca_{0.28}Ba_{0.75})_x(Sr_{0.6}Ba_{0.4})_{1-x})Nb_2O_6$ (x = 0.25, 0.5, and 0.75).

The Raman scattering technique has also been used to investigate phase transitions in the CBN and SBN compounds. For instance, Faria *et al.* [58] investigated the low-temperature phase transition in the $Sr_{0.66}Ba_{0.34}Nb_2O_6$ single crystal fibers. Speghini *et al*. [59] studied the temperature evolution of the vibration at 630 cm^{-1} to observe the ferroelectric to paraelectric phase transition in the $Sr_xBa_{1-x}Nb_2O_6$ (x = 0.33, 0.5 and 0.61) single crystals. Kasprowicz *et al*. [60, 61] investigated the ferroelectric to paraelectric phase transition in single crystals and nanopowders of $Sr_{0.5}Ba_{0.5}Nb_2O_6$ (SBN50) and (Eu,Er):SBN50.

However, the detailed analysis of the phonon spectra of CBN-like crystal at room temperature, the ferroelectric phase transition at higher-temperature as well as the crystal stability at lower-temperature have not been reported yet. Therefore, in Chapter 4 we will perform the above investigations.

1.4 Potassium tantalite niobate (KTN) crystals

Potassium tantalite niobate ($KTa_{1-x}Nb_xO_3$, hereafter KTN) crystal is an outstanding quality multi-functional crystal which presents large electro-optic and photorefractive effects. KTN crystal is usually grown from the melt and exhibits perfect thermal, chemical and mechanical properties, which is widely used in nonlinear-optic, optic storage, optical communication and photoelectric-based devices.

KTN crystal is an infinite solid solution of $KTaO_3$ (KT) and $KNbO_3$ (KN) crystals. According to the Refs. [62-64], solid solutions of KTN_x for $x \geq 0.02$ display the same sequence of phase transitions (rhombohedral ($R3m(C_{3v}^5)$) $\rightarrow$ orthorhombic ($Amm2(C_{2v}^{14})$) $\rightarrow$

tetragonal ($P4mm(C_{4v}^1)$) $\rightarrow$ cubic ($Pm3m(O_h^1)$) [65]) as pure $KNbO_3$ crystal. Therefore, the KTN crystal can exist in both paraelectric and ferroelectric phases depending on the crystal composition at room temperature. The Curie point (Tc) and the physical properties of the crystal can be adjusted by the ratio between Ta and Nb. A KTN crystal with Tc near room temperature can be grown by appropriately adjusting the composition of the raw materials.

Although the first KTN crystal was fabricated in 1950´s, it was very difficult to obtain large and good quality single crystals, which limited its technological applications. Recently, due to the crystal growth technology improvement, large and relatively good quality KTN single crystal have been successfully fabricated.

The Raman spectroscopy technique has been employed in order to study the phase transitions in KTN_x materials. For instance, in 1999 Xia *et al.* [66] studied the paraelectric (cubic) to ferroelectric (tetragonal) structural phase transition of $KTN_{0.48}$ single crystal, by analyzing the condensed soft mode ν_5, which is related to the symmetric bending vibration of O2-O3 bonds. Similar behavior of the ν_5 mode was also observed in Fe:$KTN_{0.48}$ by Xia *et al.* [67].

In 2003, Svitelskiy and Toulouse [68] investigated the coupling of translational modes to the reorientational motion of KTN_x. They showed that the coupling is responsible not only for the depolarized component of the second-order Raman spectra but also for the frequency decreasing of the transverse acoustic mode down to the third of three transitions, where reorientational motion is no longer allowed.

In 2005, Bouziane, Fontane and Ayadi [69] measured the Raman spectrum of $KTN_{0.012}$ single crystal for temperatures down to -263 ^oC. The unexpected Raman lines observed for T > -233 ^oC were attributed to the one-phonon density of states activated by the disorder induced

by the motion of Nb ions. The dependence of these lines on both temperature and electric field reveals the formation of polar clusters as a precursor effect of the polar (ferroelectric) phase.

In 2010, Bartasyte *et al*. [70] studied the sequence of phase transitions (rhombohedral to orthorhombic (*R*-*O*), orthorhombic to tetragonal (*O*-*T*), and tetragonal to cubic (*T*-*C*)) in thin films of KTN_x (x = 0.35 and 0.5) deposited on MgO and $LaAlO_3$ substrates. They observed that the phase transition temperatures were different from those reported for bulk samples. The enhancement of ferroelectricity is likely to be due to the biaxial strain in the films. They established some criteria for the identification of the phase transitions, and determined two out of three phase transitions (*C*-*T* and *T*-*O*). The *O*-*R* transition was difficult to be identified since the expected changes in the 560 cm^{-1} region are subtle and the bands could not be resolved due to band overlap.

To understand the full sequence of phase transitions undergone by highly-diluted KTN_x single crystals, we grew the KTN_x (x = 0.45, 0.50 and 0.55) crystals, and in Chapter 5 we will investigate their phase transitions.

2

ISOTOPE LITHIUM NIOBATE ($^7LiNbO_3$) CRYSTALS

2.1 Introduction

Here we report on the detailed growth of C^7LN single crystal and the characterizations of its primary properties. The X-ray, Raman, absorption and thermal techniques were used to characterize the C^7LN single crystal. The effect of Li vacancy content is analyzed by comparing the results with those obtained for near-stoichiometric lithium isotope niobate (NS^7LN) and congruent natural lithium niobate (CLN) crystals.

2.2 Experimental procedure

2.2.1 Crystal growth

The crystals were grown by Nana Zhang, Jiyang Wang, Huaijin Zhang, *et al*. in the State Key Laboratory of Crystal Materials of Shandong University (China).

(1) The crystal growth apparatus

The C^7LN single crystal was grown by the Czochraski method in a TDL model-H50AC crystal pulling apparatus as shown in Fig 2.1.

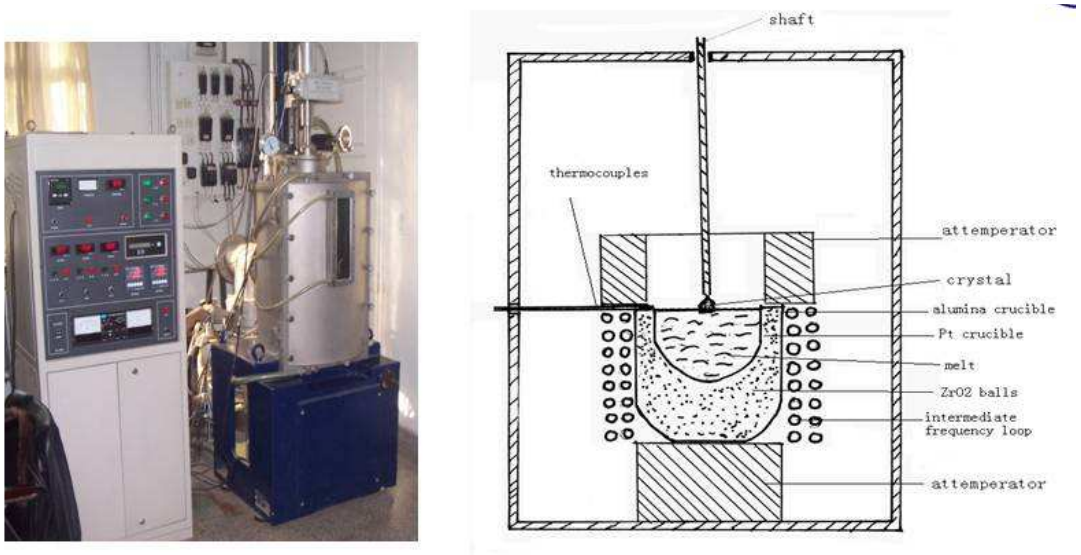

Figure 2.1. The crystal growth apparatus

(2) The synthesis of polycrystalline material

The starting materials for synthesis of C^{7}LN polycrystalline material were ^{7}LiOH (99.9%) and Nb_2O_5 (99.99%), which were mixed in 48.4/51.6 molar proportion of $^{7}Li_2O/Nb_2O_5$ according to the following reaction:

$$2\,{}^{7}LiOH + Nb_2O_5 = 2\,{}^{7}LiNbO_3 + H_2O\uparrow \quad (1)$$

^{7}LiOH has a strong chemical activity and can easily absorb H_2O and CO_2 from air to form $^{7}LiOH\cdot H_2O$ and $^{7}Li_2CO_3$. First, it must be baked at about 100 °C for at least 24 h to remove water, and then the pressed mixture was put into a platinum crucible, heated up to 450 °C , 850 °C, 1000 °C for 4 h, 4 h, 5 h, respectively, to form polycrystalline material. ^{7}LiOH is also a strong alkali and can corrode the platinum crucible, mainly at high temperatures. Therefore, we put a pure Nb_2O_5 pellet in the bottom of the mixture to prevent the contact between ^{7}LiOH and the crucible during sintering procedure.

(3) Crystal growth

A *c*-axis natural LN crystal rod (Φ 3 mm × 20 mm) was used as seed. During the growing, the pulling rate ranged from 0.3 to 0.5 mm/h and the rotation rate was kept at 5 rpm. The crystal was cooled down to room temperature in air at a rate of 30 °C/h.

For the sake of comparison, we also grew NS^7LN crystal with the similar growth procedure but the following molar proportion of raw materials ($^7Li_2O/Nb_2O_5$ = 58.5/41.5).

2.2.2 Characterizations

(1) X-ray powder diffraction (XRPD)

The phase identification of the as-grown crystal was verified using X-ray powder diffractometer (Bruker, model: Smart PPEX II) with Cu $K_{\alpha 1}$ line (λ = 1.5406 $\times 10^{-10}$ m). The unit cell parameters were calculated using LeBail method and TOPASS program.

(2) Density

The crystal density was measured using the buoyancy method at room temperature.

(3) The absorption spectrum

The absorption measurements were performed using a U-3500 Hitachi spectrophotometer in the 190-3200 nm wavelength range at room temperature.

(4) Raman spectrum

The room temperature backscattered polarized Raman spectra were recorded on a Jobin-Yvon Model T64000 triple spectrometer with a spectral resolution of 2 cm^{-1}. The instrument was equipped with a liquid-N_2-cooled charge-coupled device system. For spectral excitation, green 514.5 nm radiation from a Coherent Model Innova 70 Ar^+-ion laser operating at 30 mW was employed.

(5) Differential thermal analysis (DTA) and thermalgravimetric (TG)

The Differential thermal analysis and thermalgravimetric (DTA/TG) melting were performed on heating at a rate of 15 K/min over the room temperature to 1300 ^{o}C.

(6) Specific heat

The specific heat (C_p) measurements were performed on heating at a rate of 10 K/min using a differential scanning calorimeter (DSC822^{e}) in the 288-573 K range.

(7) The thermal expansion and diffusion measurements

The thermal expansion and diffusion coefficients were obtained using a thermal mechanical analyzer (TMA) between 298 K and 773 K with a rate of 5 K min^{-1}. The laser pulsed method was used to measure the thermal diffusion coefficients on a Nanoflash LFA 447 along the a- and c-axis.

Polished samples of good quality with dimensions 5(X) × 6(Y) × 7(Z) mm^3 were provided for Raman and thermal expansion measurements, while samples with dimensions 6×6×2 (a, b, c) mm^3 were provided for absorption and thermal diffusion experiments.

2.3 Results and discussion

2.3.1 The as-grown crystal and structure

(1) The as-grown crystal

Figure 2.2 shows the morphology of as-grown C^{7}LN and NS^{7}LN single crystals. They are transparent and free of inclusions as observed by naked eyes.

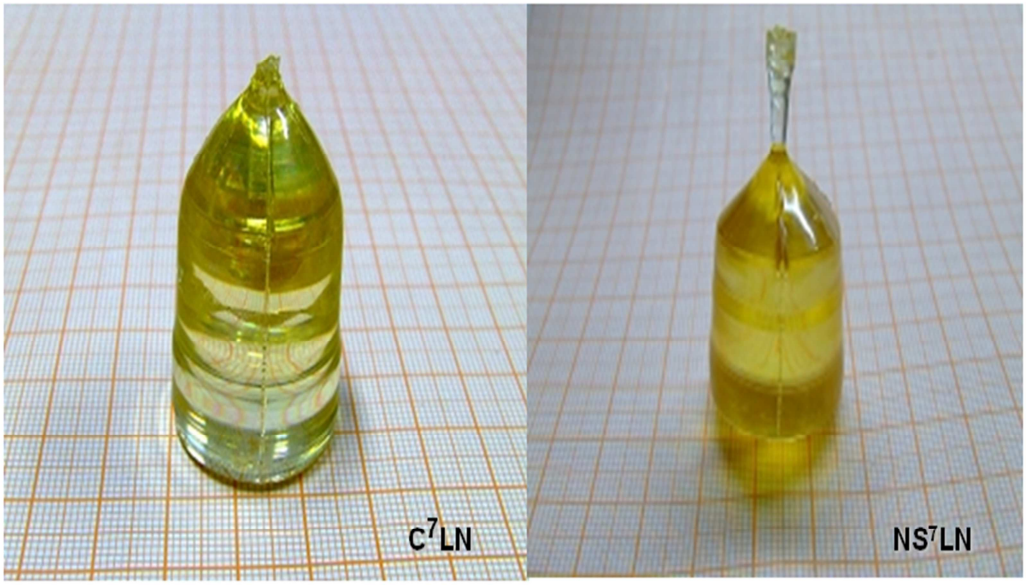

Figure 2.2. The morphology of as-grown C^7LN and NS^7LN crystals

(2) XRPD

The XRPD pattern is shown in Figure 2.3, which indicates that the as-grown crystals are single-phased (*R*3*c*) LN. The unit cell parameters and volume calculated of C^7LN and NS^7LN single crystals are $a = b = 5.1496$ Å, $c = 13.8662$ Å, V = 319.72 $Å^3$, and $a = b = 5.1540$ Å, $c = 13.8713$ Å, V = 319.11 $Å^3$, respectively.

(3) Density

The density of C^7LN and NS^7LN single crystals determined by buoyancy method at room temperature is 4.626 $g/cm^3$and 4.614 g/cm^3, respectively. The crystal density can be calculated by using the formula of $\rho = MZ/(N_A V)$, where, M is the crystal molar mass, Z is the number of molecular per unit-cell, N_A is the Avogadro constant and V is the unit-cell volume. The calculated density of C^7LN and NS^7LN single crystals is 4.588 g/cm^3 and 4.634 g/cm^3, respectively, which agree with the experiment results.

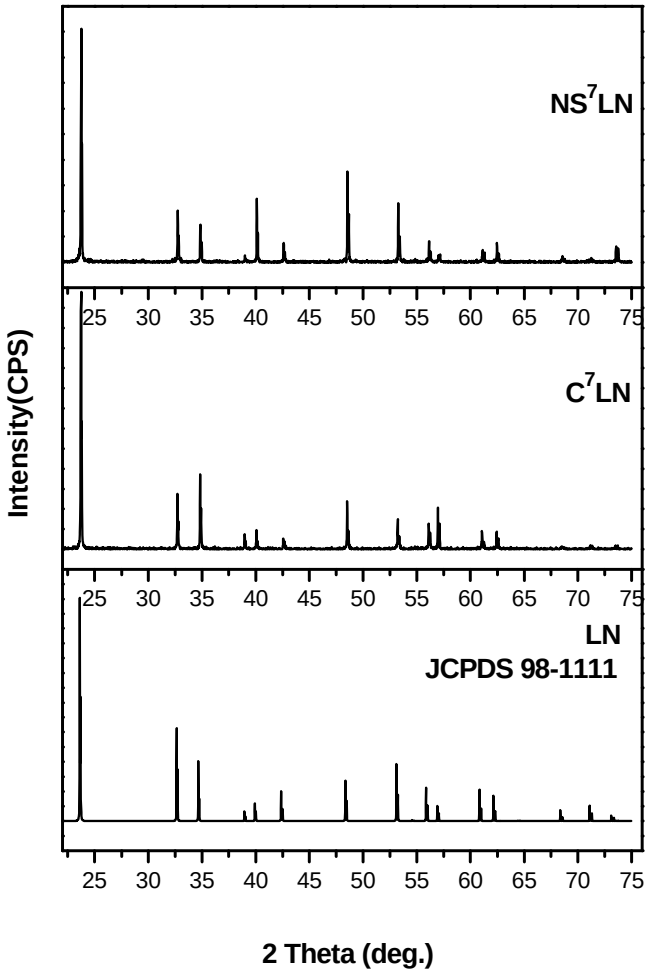

Figure 2.3. XRPD pattern of as-grown C^7LN and NS^7LN crystals

2.3.2 The spectroscopy measurements

(1) UV absorption spectrum

The LN crystal content can be obtained by the method of UV absorption edge measurements. In general, the absorption edge is defined as the wavelength corresponding to the absorption coefficients at 15 cm^{-1} and 20 cm^{-1}. The relation between the absorption edge and the Li content is given by the following formulas [71]:

$$\lambda_{15} = 321.9 - 1.579x - 5.745x^2 \text{ [71]}, \quad (2)$$

$$\lambda_{20} = 320.4 - 1.829x - 5.485x^2 \text{ [71]}, \quad (3)$$

where λ_{15} and λ_{20} are the wavelength corresponding to the absorption coefficients at 15 cm^{-1} and 20 cm^{-1}, respectively. The x value stands for the deviation of Li concentration from the congruent composition, i.e., x% = [Li]% − 48.38%. The absorption edge measured of C^7LN and NS^7LN is shown in Figs 2.4 (a) and (b), respectively, we can see that the absorption edge of C^7LN is about 325 nm (λ_{15}) while the absorption edge and of NS^7LN is 312 nm (λ_{20}), with these values we find c_{Li} (C^7LN) = 47.47% and c_{Li} (NS^7LN) = 49.46%.

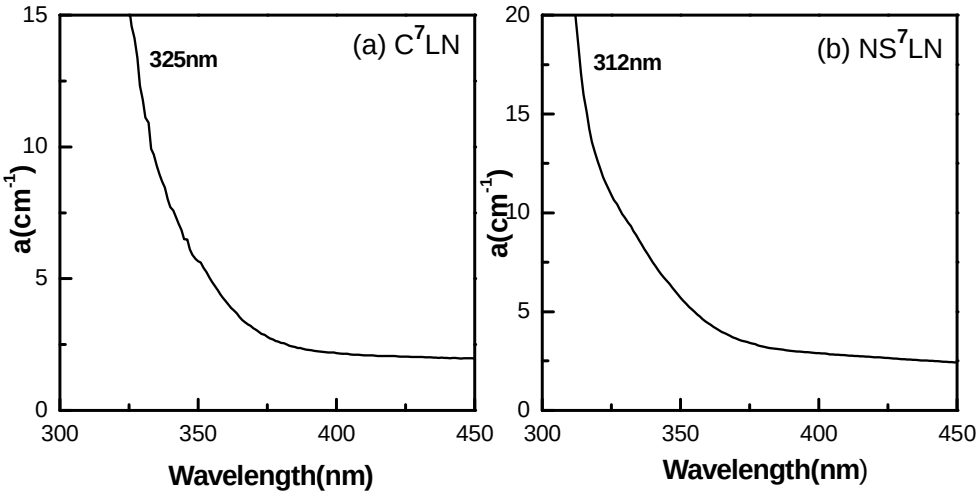

Figure 2.4. The absorption edge of (a) C^7LN and (b) NS^7LN crystals

(2) Raman spectrum

At room temperature, LN crystal exhibits *R*3c space group structure with two molecules per unit cell (Z = 2). Its Raman-active modes can be expressed as $\Gamma = 4A_1+9E$. Figure 2.5 displays the Raman spectra of C^7LN and NS^7LN crystals. According to the group theory analysis, $4A_1$(TO) and 9*E*(TO) Raman-active modes are expected in the y(zz)y and x(yz)x configurations, respectively.

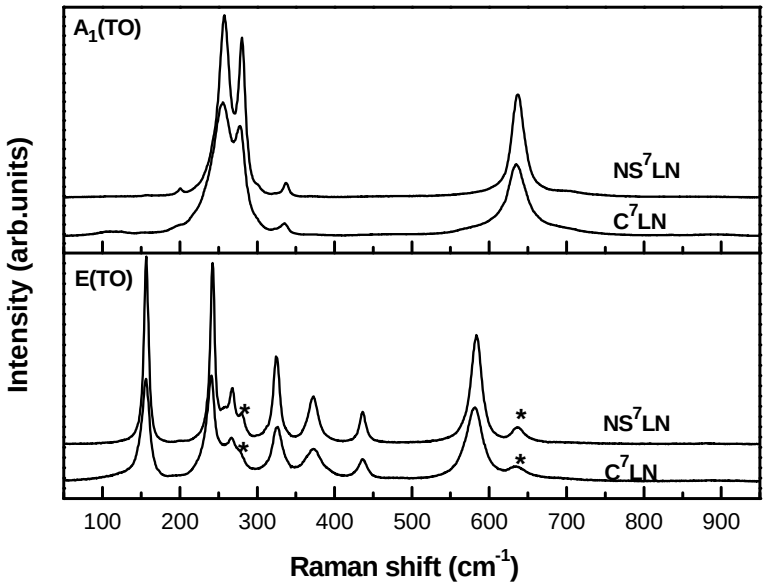

Figure 2.5. Room temperature Raman spectrum of C^7LN and NS^7LN crystals. A_1(TO) and E(TO) phonons are detected in y(zz)y and x(yz)x configurations, respectively

Schaufele and Weber [72] observed $3A_1$(TO)+$7E$(TO) modes for LN. Repelin *et al.* [14] observed $4A_1$(TO) modes and $9E$(TO) modes for ^{7}LN, and $4A_1$(TO)+$8E$(TO) modes for ^{6}LN. Lengyel *et al.* [73] observed $3A_1$(TO)+$7E$(TO) for Mg-doped LN (Mg:LN) crystals with stoichiometric, intermediate and congruent compositions. Ridah *et al.* [74] observed $4A_1$(TO)+$9E$(TO) modes for LN with different compositions. Zhang *et al.* [75] observed $4A_1$(TO)+$8E$(TO) for Er:LN, and $4A_1$(TO)+$9E$(TO) for Er:Ti:LN. Zhang *et al.* [76] observed $4A_1$(TO)+$9E$(TO) for Zn:LN.

We observed $4A_1$(TO)+$7E$(TO) modes for both C^7LN and NS^7LN, as listed in Table 2.1 along with those of the aforementioned references, and all the peaks observed were decomposed using Gaussian-Lorentzian functions and a homemade pc-based program. The modes appearing at 280 and 630 cm^{-1} and marked with an asterisk in the yz polarization are likely to be a leakage from the zz polarization [73]. We observed that the vibration modes of

C^7LN are broader than those of NS^7LN, reflecting the effect of Li vacancy content. Recently, Shi *et al.* [77] used the Raman spectroscopy technique to investigate lithium tantalite ($LiTaO_3$) crystals with different compositions. By comparing the data obtained for the congruent and near-stoichiometric crystals, they observed differences in the shape and the number of Raman peaks. They also observed that the mode linewidth (Γ) continually decreases with increasing Li content. There exist many defects due to the Li vacancy and anti-site Ta ion for congruent $LiTaO_3$ crystal. When the ratio Li/Ta increases, the number of intrinsic defect decreases.

To obtain the number of Li vacancy (V_{Li}) we employ the model proposed by Iyi *et al.* [9], where the formula for LN is given by $[Li_{1-5x}Nb_x(V_{Li})_{4x}]\ NbO_3$. According to Ref.[71], Γ can be used to estimate the crystal composition. By considering the unambiguously identified *E*(TO) mode at around 156 cm^{-1}, the Li concentration (c_{Li}) can be obtained from the following equation [71]

$$c_{Li} = 53.03\text{-}0.4739\Gamma \qquad (4)$$

Table 2.1. Frequency (cm^{-1}) and linewidth, Γ(cm^{-1}), in parenthesis, of the Raman-active modes for C^7LN and NS^7LN crystals.

	E(TO)									A_1(TO)				
C^7LN	156	…	240	268	326	373	436	581	…	255	279	335	635	Present work
	(12)	…	(13)	(27)	(16)	(26)	(14)	(26)	…	(33)	(13)	(10)	(33)	
NS^7LN	157	…	242	267	325	372	436	583	…	258	280	337	637	Present work
	(7)	…	(7)	(18)	(10)	(16)	(10)	(17)	…	(17)	(11)	(8)	(20)	
LN	152	…	239	266	321	369	430	580	…	…	…	…	…	Ref.[72]
^7LN	155	180	238	265	325	371	431	582	610	255	276	334	633	Ref.[14]
^6LN	155	180	238	…	333	388	431	581	610	257	294	364	630	Ref.[14]
LN	153	177	238	264	322	370	432	580	610	…	…	…	…	Ref.[74]
Er:LN	151	…	237	262	322	366	431	579	630	250	272	328	631	Ref.[75]
Er:Ti:LN	152	182	238	263	322	369	431	580	629	253	275	333	633	Ref.[75]
Zn:LN	155	236	263	314	365	428	614	665	878	251	274	334	630	Ref.[76]

From the data listed in Table 2.1, we have c_{Li} (C^7LN) = 47.34% and c_{Li} (NS^7LN) = 49.72%, which are in good agreement with the results determined by UV absorption edge method. Using the results for c_{Li} (C^7LN) and c_{Li} (NS^7LN), the chemical formula for C^7LN and NS^7LN reads: $[Li_{0.91}Nb_{0.02}(V_{Li})_{0.07}]NbO_3$ and $[Li_{0.99}Nb_{0.002}(V_{Li})_{0.008}]NbO_3$, respectively. We observe that $V_{Li}(C^7LN)$ is greater than $V_{Li}(NS^7LN)$, accounting for the broader modes observed in the Raman spectra of C^7LN.

2.3.3 The thermal properties measurements

(1) DTA/TG curves

The DTA/TG curves of C^7LN and NS^7LN single crystals are shown in Figs. 2.6 (a) and (b), respectively. The sharp peak appearing in the DTA curve indicates that the melting point of as-grown C^7LN and NS^7LN crystal is 1218 ^oC and 1223 ^oC, respectively. The TG curves indicate that the as-grown crystals are stable over the room temperature to 1300 ^oC with no mass variation.

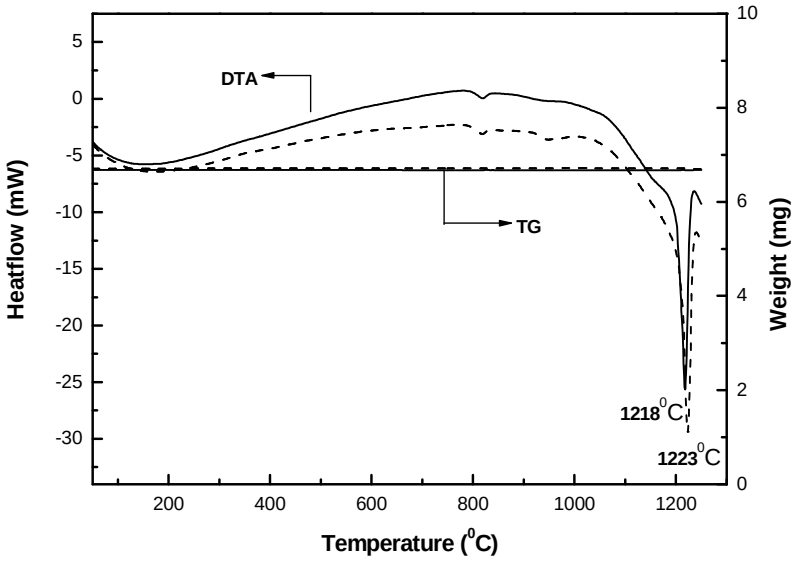

Figure 2.6. DTA/TG curves of C^7LN (solid) and NS^7LN (dashed) crystals

(2) The specific heat measurements

The specific heat (C_p) is an important thermal parameter, which reflects the thermal stability and affects the crystal damage threshold [78]. The specific heat value of as-grown C^7LN as well as NS^7LN is plotted in Figs 2.7, and the measurements reveal that C_p varies slightly in the temperature range 300-550 K, at 300 K, we have $C_p(C^7LN) = 0.5995\ Jg^{-1}K^{-1}$ and $C_p(NS^7LN) = 0.7280\ Jg^{-1}K^{-1}$.

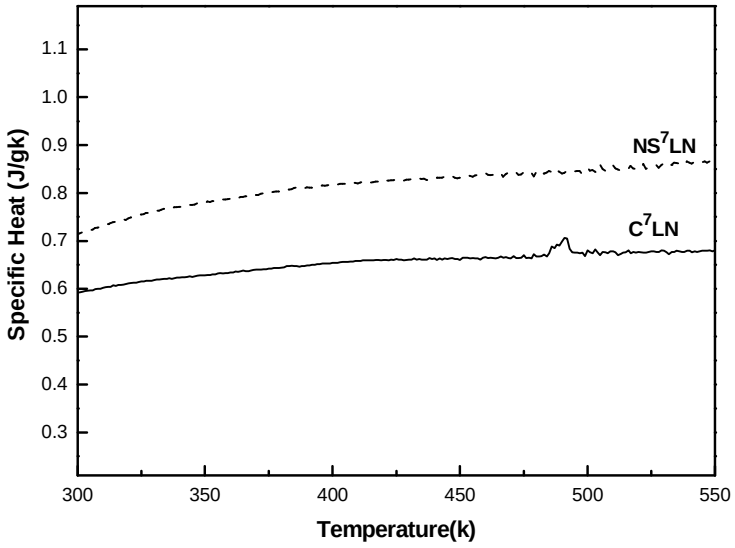

Figure 2.7. The specific heats of C^7LN (solid) and NS^7LN (dashed) crystals

(3) The thermal expansion measurements

The thermal expansion coefficient is also an important thermal parameters that influences the fracture of crystal material. Figures 2.8 (a) and (b) show the temperature dependent behavior of the thermal expansion and thermal expansion coefficients (α_a and α_c) for C^7LN (solid line) and NS^7LN (dashed line) crystals, respectively. The average thermal expansion coefficients are $\alpha_a = 13.2 \times 10^{-6}\ K^{-1}$ and $\alpha_c = 1.8 \times 10^{-6}\ K^{-1}$ for C^7LN and $\alpha_a = 13.5 \times 10^{-6}\ K^{-1}$ and $\alpha_c = 2.1 \times 10^{-6}\ K^{-1}$ for NS^7LN, respectively.

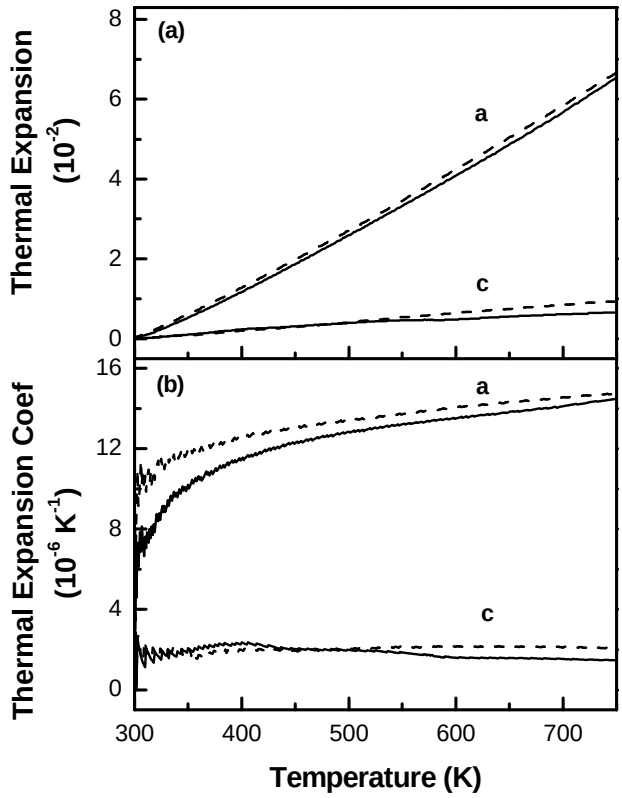

Figure 2.8. (a) Thermal expansion and (b) thermal expansion coefficients of C^7LN (solid) and NS^7LN (dashed) crystals

(4) The thermal diffusion and thermal conductivity

Figure 2.9 (a) shows the behavior of the thermal diffusion coefficients (λ_a and λ_c), which is anisotropic and decreases with increasing temperature. At 300 K, λ_a = 0.84 mm^2s^{-1} and λ_c = 1.1 mm^2s^{-1} for C^7LN and λ_a = 1.37 mm^2s^{-1} and λ_c = 1.62 mm^2s^{-1} for NS^7LN.

The thermal conductivity, κ, can be calculated according to the equation

$$\kappa = \lambda \rho C_p \quad (5)$$

where λ, ρ, C_p are the thermal diffusion coefficient, density, and specific heat, respectively. The calculated thermal conductivities are also plotted in Fig 2.9 (b), and the values at 300 K

are κ_a = 2.55 $Wm^{-1}K^{-1}$ and κ_c = 3.1 $Wm^{-1}K^{-1}$ for C^7LN, and κ_a = 4.25 $Wm^{-1}K^{-1}$ and κ_c = 5.25 $Wm^{-1}K^{-1}$ for NS^7LN, respectively.

All the thermal parameters of C^7LN and NS^7LN are listed in Table 2.2, where we also list the data of natural CLN obtained from Ref. [79].

Table 2.2. Experimental results of C^7LN, NS^7LN and CLN crystals. Chemical formula is calculated based on Li vacancy model. ($[Li_{1-5x}Nb_x(V_{Li})_{4x}]NbO_3$, where V_{Li} means vacancy at Li-site). The values of specific heat (C_p), thermal diffusion coefficients (λ) and thermal conductivity (κ) were determined at 300 K, the average thermal expansion coeffients (α) are obtained between 298-773 K. Data for CLN were obtained from Ref.[79].

	C^7LN	NS^7LN	CLN
[Li]/[Li]+[Nb] (100%)	47.34	49.72	48.53
Chemical formula	$[Li_{0.91}Nb_{0.02}(V_{Li})_{0.07}]NbO_3$	$[Li_{0.99}Nb_{0.002}(V_{Li})_{0.008}]NbO_3$	$[Li_{0.95}Nb_{0.01}(V_{Li})_{0.04}]NbO_3$
C_p ($Jg^{-1}K^{-1}$)	0.5995	0.7280	0.6010
α ($\times 10^{-6}K^{-1}$)	α_a = 13.2 , α_c = 1.8	α_a = 13.5 , α_c = 2.1	α_a = 16.1 , α_c = 3.3
λ (mm^2s^{-1})	λ_a = 0.84 , λ_c = 1.1	λ_a = 1.37 , λ_c = 1.62	λ_a = 1.17 , λ_c = 1.26
κ (W/mK)	κ_a = 2.55 , κ_c = 3.1	κ_a = 4.45 , κ_c = 5.25	κ_a = 3.28 , κ_c = 3.54
	Present work	Present work	Ref.[79]

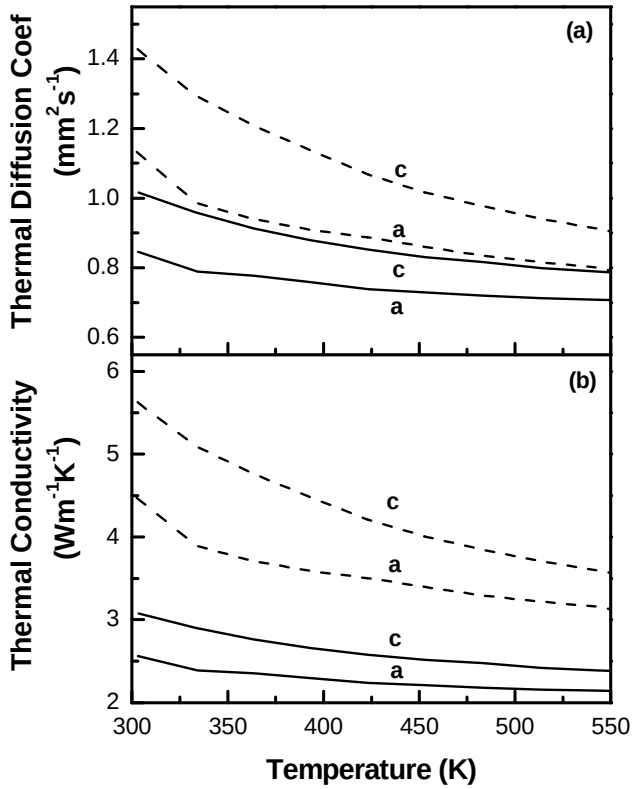

Figure 2.9. (a) Thermal diffusion coefficients and (b) thermal conductivity curves of C^7LN (solid) and NS^7LN (dashed) crystals

According to Ref.[80], κ can also be written as

$$\kappa = \rho C_p \upsilon L/3, \quad (6)$$

where υ is the constant sound velocity, and L is phonon mean free path (MFP). Phonon scattering in a solid consists of four processes involving collisions between phonons and (a) phonons, (b) defects, (c) free electrons, and (d) boundaries of the system [80]. Since L (and κ) decreases with increasing the number of defects, the collisions between phonons and defects explain why the thermal parameters of C^7LN are smaller than that of NS^7LN and CLN.

2.4 Conclusion

For future investigations on the defect structure of LN using neutron scattering technique, we successfully grew C^7LN and NS^7LN crystal and carried out series of primary measurements. The XRPD result showed the as-grown crystals of *R*3*c* LN phase structure, the crystal theory and experimental densities were determined, the UV absorption edge method and Raman mode method were used to determine the crystal contents, the DTA results gave the crystal melting points and the TG results indicated that the crystal is stable over the room temperature to the melting points, the crystals specific heats, thermal expansion, thermal diffusion and thermal conductivity values were determined and calculated.

The Raman modes of C^7LN are broader than those of NS^7LN, reflecting the disorder induced by the larger amount of Li vacancies on the *R*3*c* phase of C^7LN. This disorder also accounts for the lower values of the thermal parameters λ and κ of C^7LN as compared to those of NS^7LN and natural CLN.

3

MIXED-VANADATE ((Nd,Yb):$Y_xGd_{1-x}(VO_4)$) CRYSTALS

3.1 Introduction

Here we used Raman spectroscopy to investigate the extent of the modification of the $GdVO_4$ phonons due to the doping of the Gd site by Y, Yb, and Nd. We observed that the wavenumber of most of the vibrations increases when Y replaces for Gd in the (Nd,Yb):$Y_xGd_{1-x}(VO_4)$ crystals, while it remains approximately constant when Yb replaces for Gd in the Yb:$Gd(VO_4)$ crystal. Besides providing information about the disorder on the zircon structure as x increases, the Raman spectroscopy yields information about the maximum phonon energy, used in the analysis of loss mechanism of a given electronic transition (lifetime). Finally, we tried to build up the one-phonon model to describe the dependence of the wavenumbers on x.

3.2 Experimental procedure

3.2.1 Crystal growth

The crystals were grown by Jiyang Wang, Huaijin Zhang, *et al*. in the State Key Laboratory of Crystal Materials of Shandong University (China).

(1) The crystal growth apparatus

Single crystals of (Nd,Yb):$Y_xGd_{1-x}(VO_4)$ were prepared following the procedure as described in Refs [81-83]. The crystals were grown by the Czochraski method in the DJL-400 pulling apparatus, the temperature control apparatus was a EUROTHERM2604 controller/programmer with a precision of ± 0.1 °C. The iridium crucible was heated using a 2 kHz intermediate frequency heater. The craw distance of the pulling apparatus was less than 1 μm.

(2) The synthesis of polycrystalline material

The starting materials for synthesis polycrystalline material were V_2O_5, Gd_2O_3, Y_2O_3, Yb_2O_3 and Nd_2O_3 with 99.99% purity, which were grind, weighted according to the appropriate molar proportion, and then the mixture were placed into a Pt crucible and heated at 850 °C for 7 h. The obtained materials were grind and mixed again, and then pressed into pellets, and heated at 1150 °C for 7-10 h, finally formed the mixed vanadate polycrystalline.

(3) Crystal growth

An *a*-axis Nd:$GdVO_4$ crystal rod (3 mm × 3 mm × 20 mm) was used as seed. The crystals were finally grown in an atmosphere N_2+O_2 (O_2 2% by volume). During the growing, the pulling rate ranged from 0.5 to 1 mm/h and the rotation rate varied at 10-30 rpm. After the crystal reached the ideal diameter, it was cooled down to room temperature at a rate of 60-80 °C/h.

3.2.2 Characterizations

(1) X-ray fluorescence (XRF)

The concentrations of Nd^{3+}, Gd^{3+}, Y^{3+}, and Yb^{3+} ions were measured by the X-ray fluorescence (XRF) analysis method using a X-ray Fluorescence Spectrometer (Japan, model: S/max3080E2).

(2) XRPD

The crystal structures were measured using a X-ray powder diffractometer (XRPD) (Bruker, model: Smart PPEX II) with Cu $K\alpha_1$ line (λ = 1.5406 $\times 10^{-10}$ m). The unit cell parameters were calculated using LeBail method and TOPASS program.

(3) Raman spectra

We used the same setup described in Chapter 2. Scattering geometries for the spectra listed in the text, tables and figures follow the usual Porto's notation [80]. The typical crystal selected for the Raman study consisted of a parallelepiped, whose average dimensions were 6 x 6 x 2 mm^3.

3.3 Results and discussion

3.3.1 Crystal compositions and structure

(1) The crystal contents

The three families of rare-earth vanadates investigated, namely: (i) *y*Nd:$Y_xGd_{1-x}(VO_4)$, (ii) *y*Yb:$Gd(VO_4)$ and (iii) *y*Yb:$Y_xGd_{1-x}(VO_4)$ are listed in Table 3.1.

Table 3.1. Chemical formula for *y*(Nd,Yb):$Y_xGd_{1-x}(VO_4)$ crystals

*y*Nd:$Y_xGd_{1-x}VO_4$	*y*Nd:$GdVO_4$	*y*Yb:$Y_xGd_{1-x}VO_4$
Nd(0.5 at.%):$Y_{0.17}Gd_{0.83}VO_4$	Yb(0.8 at.%):$GdVO_4$	Yb(0.48 at.%):$Y_{0.30}Gd_{0.70}VO_4$
Nd(0.5 at.%):$Y_{0.37}Gd_{0.63}VO_4$	Yb(1.5 at.%):$GdVO_4$	Yb(0.71 at.%):$Y_{0.41}Gd_{0.59}VO_4$
Nd(0.5 at.%):$Y_{0.53}Gd_{0.47}VO_4$	Yb(2.0 at.%):$GdVO_4$	Yb(0.92 at.%):$Y_{0.58}Gd_{0.42}VO_4$
Nd(0.5 at.%):$Y_{0.63}Gd_{0.37}VO_4$	Yb(2.5 at.%):$GdVO_4$	Yb(1.18 at.%):$Y_{0.74}Gd_{0.26}VO_4$
Nd(0.5 at.%):$Y_{0.70}Gd_{0.30}VO_4$	Yb(3.5 at.%):$GdVO_4$	Yb(1.35 at.%):$Y_{0.87}Gd_{0.13}VO_4$
Nd(0.5 at.%):$Y_{0.81}Gd_{0.19}VO_4$		

(2) XRPD

The XRPD result of *y*Nd:$Y_xGd_{1-x}(VO_4)$ crystals is plotted in Fig 3.1, and the unit cell parameters calculated [81] varying with contents are plotted in Fig 3.2. From the XRPD

results, we observed that all as-grown (Nd,Yb):$Y_xGd_{1-x}(VO_4)$ crystals possess the tetragonal (zircon-type) structure belonging to the D_{4h}^{19} space group.

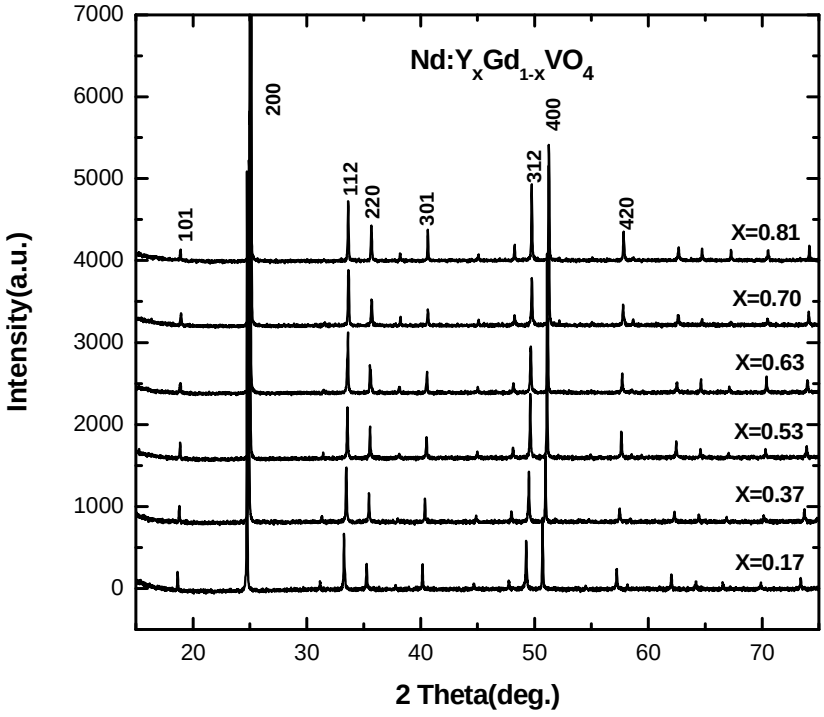

Figure 3.1. The XRPD result of *y*Nd:$Y_xGd_{1-x}(VO_4)$ crystals

(3) Crystal structure

Kolitsch and Holstam [85], showed that the $REVO_4$ (RE = Nd, Yb, Y, and Gd) are isostructural, exhibiting a tetragonal (zircon-type) structure belonging to D_{4h}^{19} space group with four molecules per unit cell (Z = 4), where RE and VO_4 occupy D_{2d} crystallographic sites. In Ref. [86], Isasi *et al*. showed that in the mixed $Y_xGd_{1-x}(VO_4)$, the rare-earths Y and Gd share the same D_{2d} crystallographic site, and the unit cell structure of $REVO_4$ family crystals are shown in Fig 3.4.

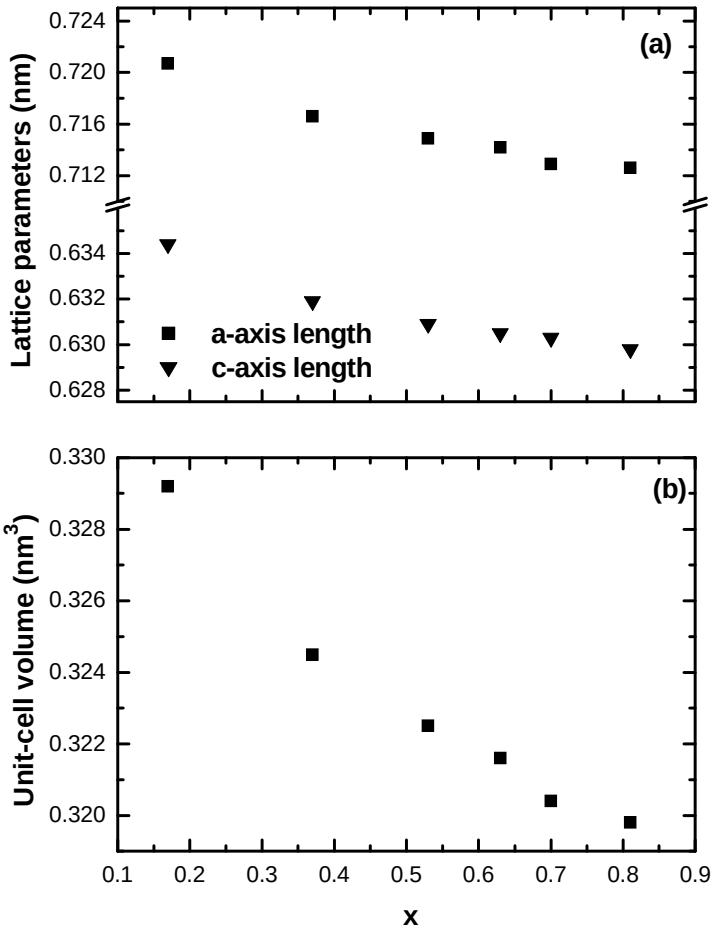

Figure 3.2. The unit cell parameters of yNd:$Y_xGd_{1-x}(VO_4)$ crystals varying on the crytal contents

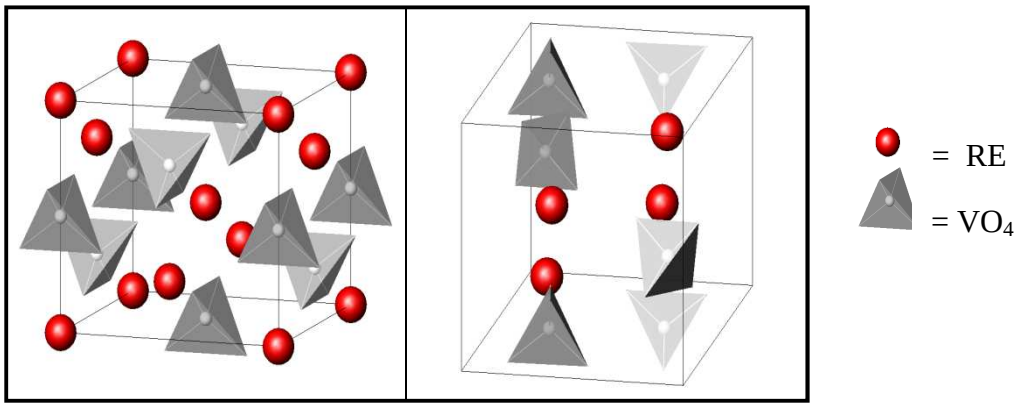

Figure 3.3. The unit cell structure of $REVO_4$ crystals

3.3.2 Raman spectrum

By considering that the zircon structure is composed of two sublattices of RE^{3+} (or RE'/RE") ions and VO_4^{3-} ''molecules'', and using the group theory analysis the Raman-active modes can be decomposed in terms of the irreducible representations of the D_{4h} point group as $\Gamma = A_{1g}(\nu_1, \nu_2)+B_{1g}(2T, \nu_3, \nu_4)+B_{2g}(\nu_2)+E_g(2T,R, \nu_3, \nu_4)$, where ν_i (i = 1,…,4) correspond to the internal modes of the VO_4 tetrahedron, and T/R corresponds, respectively, to the translational (T) or rotational (R) motion involving both the RE and VO_4 ions.

(1) Nd:$Y_xGd_{1-x}(VO_4)$ crystals

Figures 3.4 (a)-(d) show the room temperature Raman spectra of Nd:$Y_xGd_{1-x}(VO_4)$ for (zz), (xx), (zx) and (xy) polarizations, respectively. These polarizations yield the Raman modes of A_{1g}, A_{1g}+B_{1g}, E_g, and B_{2g} symmetry, respectively. All the peaks observed were decomposed using Gaussian-Lorentzian functions and a homemade pc-based program.

For x = 0.0, Fig. 3.4 (a) shows the two A_{1g} modes predicted by the group theory analysis. They correspond to the symmetric bending (ν_2) at 379 cm^{-1} and the symmetric stretching (ν_1) at 885 cm^{-1}.

It should be noted that the $A_{1g}(\nu_2)$ vibration mode exhibits an inhomogeneous splitting (Δ~11 cm^{-1}) similar to those observed in Ref. [87] for Nd:$GdVO_4$. This splitting has been observed even for pure $GdVO_4$ [88]. Let A and B be the low- and high-frequency components of the A_{1g} (ν_2) doublet with integrated intensities I_A and I_B, respectively. As x increases, Δ and I_B/I_A decrease. In Ref. [88] the splitting of the $A_{1g}(\nu_2)$ mode over a wide temperature range 14-800 K was investigated. The splitting observed was associated with the thermally activated process of disorientation of the VO_4 groups in the zircon structure.

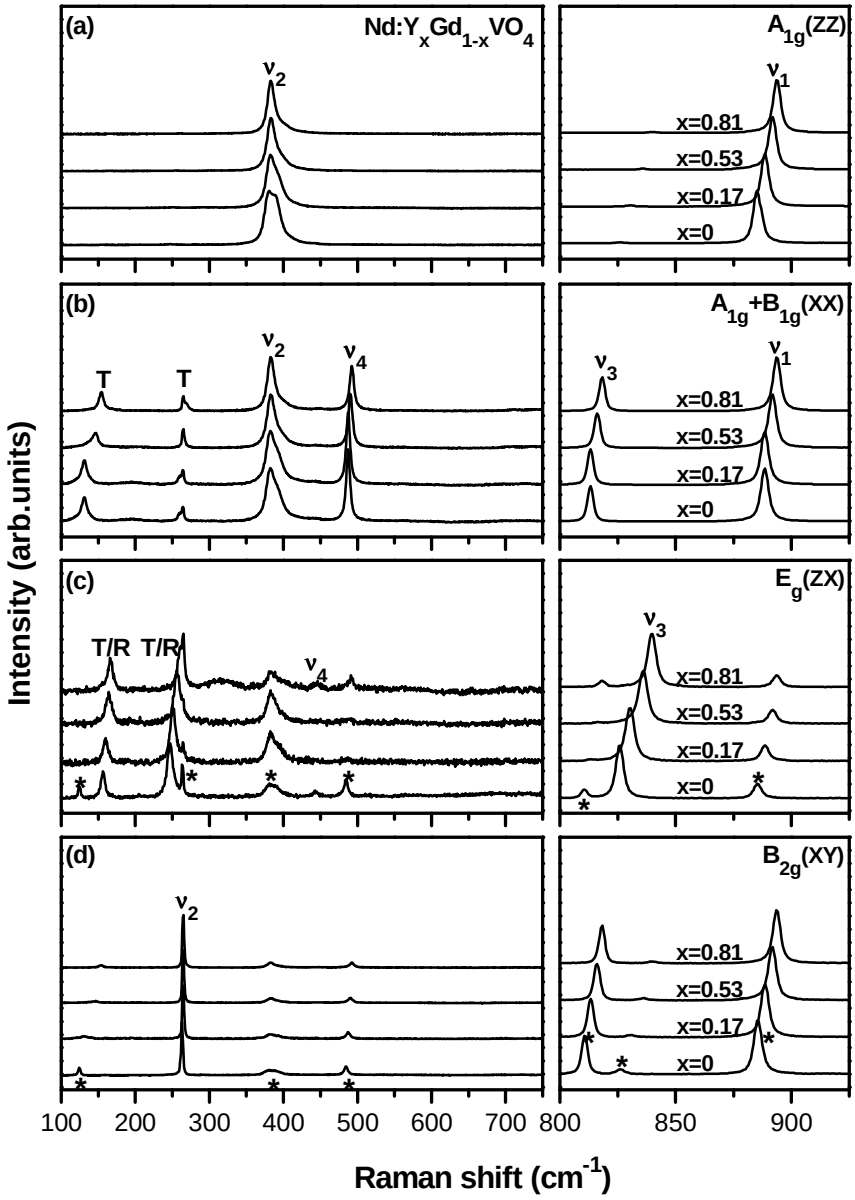

Figure 3.4. Room temperature polarized Raman spectra of Nd:$Y_xGd_{1-x}VO_4$ (x = 0.0, 0.17, 0.53, and 0.81), recorded in different polarizations: (a) (zz), (b) (xx), (c) (zx) and (d) (xy)

Similar splitting was observed for $TbVO_4$ when P replaces for V [89]. For pure $TbVO_4$ the structure has an exact translational symmetry and no splitting of the $A_{1g}(\nu_2)$ is observed, indicating that the VO_4 tetrahedral are well oriented. However, for mixed $Tb(V_{1-x}P_x)O_4$ crystals the local structure could a priori differ from the average tetragonal structure due to the random distribution of VO_4 and PO_4 groups in the D_{2d} sites. So, while the Tb sublattice retains to a good approximation, its translational symmetry, the $(V, P)O_4$ sublattice does not. In either case, the disorder in the distribution of VO_4 tetrahedral leads to the appearance of the $A_{1g}(\nu_2)$ doublet observed for some rare-earth orthovanadates.

Figure 3.4 (b) shows, in addition to the A_{1g} modes, the four B_{1g} modes expected. We assign the asymmetric stretching (ν_3) mode at 810 cm^{-1} and the asymmetric bending (ν_4) at 485 cm^{-1}. The modes at 125 and 263 cm^{-1} are related to *T*-like vibrations. Of the five expected E_g modes, we observe (Fig. 3.4 (c)) four modes at 156, 247, 443, and 826 cm^{-1}. The modes at 443 and 826 cm^{-1} are assigned as ν_4 and ν_3 vibrations, respectively. The remaining two modes at 156 and 247 cm^{-1} are likely to involve *R*- and/or *T*-like motions of the atoms. In Fig. 3.4 (d) we observe an intense vibration at 263 cm^{-1} corresponding to the ν_2 mode with B_{2g} symmetry. We recall that, according to Ref. [90], the modes $R(E_g)$, $T(B_{1g})$, and $\nu_2(B_{2g})$ have similar wavenumbers. The calculated ratio between the wavenumbers corresponding to the $\nu_2(B_{2g})$ and $T(B_{1g})$ modes is 1.03, while from our measurements we have 1.0. The asterisks indicate leakage from other polarizations, since the $REVO_4$ compounds are known to exhibit a relatively large birefringence (> 0.2).

The wavenumbers observed for x = 0.0 agree with those reported in Refs. [38] and [88] for $GdVO_4$. The Raman results indicate that the phonon spectra of Nd:$GdVO_4$ exhibits a relatively small alteration, suggesting that the $GdVO_4$ lattice is largely insensitive to Nd doping, at least for a Nd concentration of 0.005. In going from $NdVO_4$ to $GdVO_4$ the

wavenumbers of the internal VO_4 modes increases by 1.7% on average [45], while the observed shift for $Nd_{0.005}$:$GdVO_4$ is 0.15%.

The wavenumbers observed are listed in Table 3.2, where we also list the wavenumbers of Nd:YVO_4 [87], which are similar to those of YVO_4 [88, 91].

Table 3.2. Wavenumbers (cm^{-1}) and symmetry assignment of y(Nd,Yb):$Y_xGd_{1-x}VO_4$

Crystal	Content	Internal modes							External modes			
		A_{1g} (ν_1)	E_g (ν_3)	B_{1g} (ν_3)	B_{1g} (ν_4)	E_g (ν_4)	A_{1g} (ν_2)	B_{2g} (ν_2)	B_{1g}	E_g	E_g	B_{1g}
Nd:$Y_xGd_{1-x}VO_4$	x = 0.00	885	826	810	485	...	379	263	263	247	156	125
	x = 0.17	888	830	813	487	...	382	265	263	251	160	131
	x = 0.37	890	833	815	489	...	383	265	264	254	162	138
	x = 0.53	892	836	816	490	...	383	265	265	256	164	145
	x = 0.63	892	837	817	491	...	383	265	265	258	165	148
	x = 0.70	893	838	817	492	...	382	265	265	259	165	150
	x = 0.81	894	840	818	492	...	383	265	266	262	166	154
	x = 1.00	894	842	819	493	...	383	264	264	264	167	161
yYb:$GdVO_4$	y = 0.8 at.%	885	826	810	485	443	379	263	263	247	156	125
	y = 1.5 at.%	886	826	811	485	443	379	263	263	247	157	125
	y = 2.0 at.%	886	826	811	485	444	380	263	263	247	157	124
	y = 2.5 at.%	886	827	811	485	444	380	263	263	247	157	124
	y = 3.5 at.%	886	827	811	485	444	380	263	263	248	157	124
yYb:$Y_xGd_{1-x}VO_4$	y = 0.48 at.% x = 0.30	889	832	814	488	...	382	264	264	253	160	135
	y = 0.71at.% x = 0.41	890	834	814	489	...	382	264	264	254	161	140
	y = 0.92 at.% x = 0.58	891	836	816	490	...	383	264	264	257	163	146
	y = 1.18 at.% x = 0.74	892	838	816	491	...	382	264	264	259	165	151
	y = 1.35 at.% x = 0.87	892	839	817	491	...	382	263	263	261	166	155

The observed wavenumbers for the compounds as a function of doping content are plotted in Figs 3.5 (a), when x goes from 0 to 1, most of these modes shift towards higher wavenumbers. The wavenumber of the internal $\nu_1(A_{1g})$, $\nu_3(E_g)$, $\nu_3(B_{1g})$, $\nu_4(B_{1g})$, and $\nu_2(A_{1g})$ modes, and external E_g (156 and 247 cm^{-1}) and B_{1g} (125 cm^{-1}) modes increase, while that of the external B_{1g} (263 cm^{-1}) mode remains practically constant.

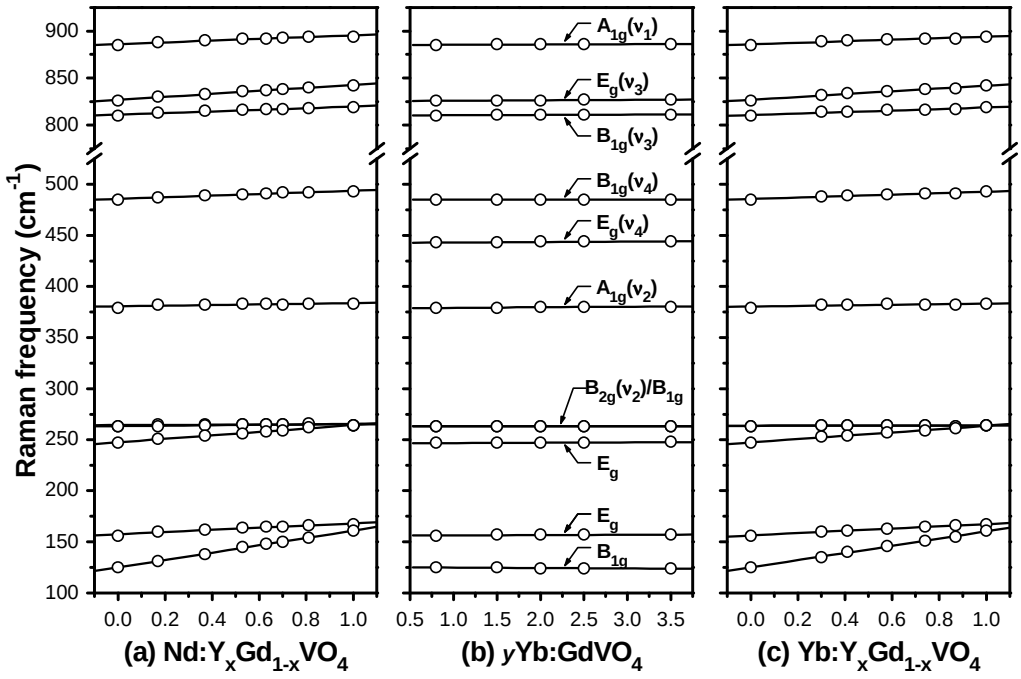

Figure 3.5. Observed wavenumbers for the compounds as a function of doping content

The hardening of the internal mode wavenumbers was first explained as resulting from the RE contraction, which would lead to a closer packing of the $(PO_4)^{3-}$ units as one proceeds from monazite-type $LaPO_4$ to zircon-type $LuPO_4$ and a shortening of the P-O distances to yield higher wavenumbers [92]. However, crystallographic studies of the $REPO_4$ series performed by Beall *et al*. [93], Mullica *et al*. [94-96], and Ni *et al*. [97] have shown that the length of the RE-O bonds decreases rather than that of the P-O separation when *Z* increases.

Usually, the PO_4 tetrahedral are bonded very tightly, and so it is unlikely that they can be deformed when the crystal is heated or under pressure [98].

Such variations also occur for the $REVO_4$ compounds, where the V-O distance decreases by 0.2%, while the distance RE-O is reduced by 6% on average in proceeding from La to Lu [45]. This implies that the crystal lattice is contracting in a manner that keeps almost constant the size of the VO_4 tetrahedron.

In Ref. [81] it is shown that the crystal lattice of the system $Nd_{0.005}:Y_xGd_{1-x}(VO_4)$ contracts when x goes from 0 to 1. In accordance with Refs. [99, 100], the RE-O distance is reduced by 1.7% on average when Y replaces for Gd, while the V-O distances increase by 0.4%. This indicates that the increase in the wavenumber of the internal modes is related to the decrease of the RE-O distance due to the lattice contraction, which leads to an increase in the energy of the VO_4 tetrahedron yielding higher stretching and bending wavenumbers [45].

Three out of the four external modes also shift towards higher wavenumbers as *Z* increases. This effect is also related to the overall lattice contraction (~4%) when x goes from 0 to 1 [81]. The wavenumber of the B_{1g} mode at ~263 cm^{-1} remains practically constant, since it is primarily associated with the VO_4 motion [89].

(2) *y*Yb:Gd(VO_4) crystals

Due to the lack of luminescence quenching, larger amounts of Yb^{3+} than Nd^{3+} can be incorporated into $GdVO_4$ lattice for high pump power pulsed lasers, we have grown *y*Yb:Gd(VO_4) crystals, with y = 0.008, 0.015, 0.020, 0.025, and 0.035. Their Raman spectra are shown in Figs 3.6 (a)-(d), and the observed wavenumbers for the compounds as a function of doping content are plotted in Figs 3.5 (b).

In addition to the modes observed in Figs. 3.4(a)-(d), we observed a vibration at 444 cm^{-1} which is assigned to the ν_4 mode with E_g symmetry [88]. No changes were observed in

the Raman spectra for different Yb^{3+} concentrations, indicating that Yb^{3+} doping produces no significant modification in the zircon-type structure of $GdVO_4$ crystal. The wavenumbers of the Yb:$GdVO_4$ compounds are also listed in Table 3.2.

This result agrees with those previously reported by Hu *et al.* [101] who observed from the X-ray powder diffraction technique, that the Yb^{3+} ions do not alter the essential zircon-type structure of $GdVO_4$ even for doping levels as high as 0.17. For y = 0.0646, the variation of the unit cell volume is only ~0.5%.

(3) yYb:$Y_xGd_{1-x}(VO_4)$ crystals

Having realized that Yb^{3+} doping at the Gd site does not change the lattice structure, the modification in the Raman spectra of yYb:$Y_xGd_{1-x}(VO_4)$ observed from Figs. 3.7 (a)-(d), should be mainly due to the Y doping as observed for Nd:$Y_xGd_{1-x}(VO_4)$. The wavenumbers of yYb:$Y_xGd_{1-x}VO_4$ as a function of Y content are also listed in Table 3.2 and plotted in Fig. 3.5 (c), where we observed that most of the observed wavenumbers in the system y(Nd,Yb):$Y_xGd_{1-x}(VO_4)$ exhibit a one-phonon-like behavior, as expected for $REVO_4$ compounds with zircon-type structure.

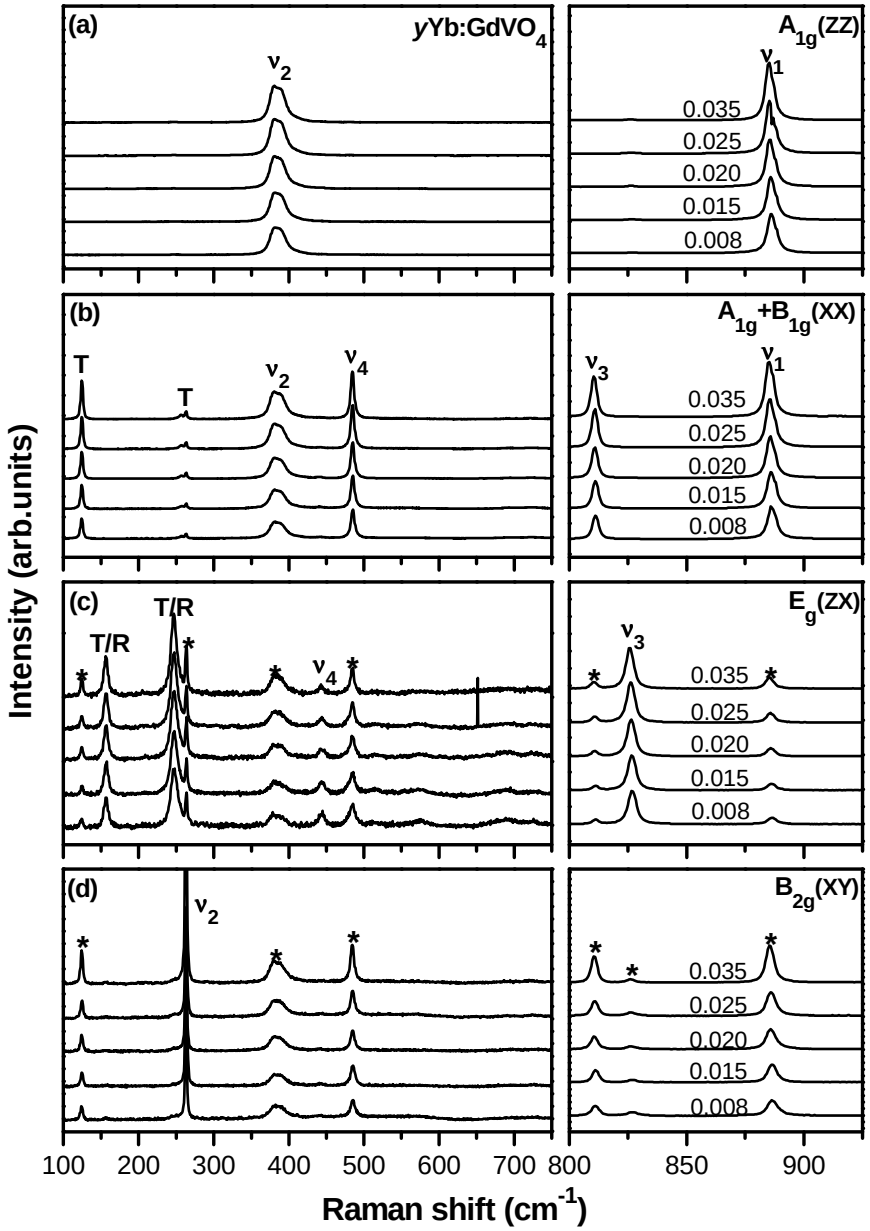

Figure 3.6. Room temperature polarized Raman spectra of *y*Yb:$GdVO_4$ (*y* = 0.008,0.015, 0.020, 0.025, and 0.035), recorded in different polarizations: (a) (zz), (b) (xx), (c) (zx) and (d) (xy)

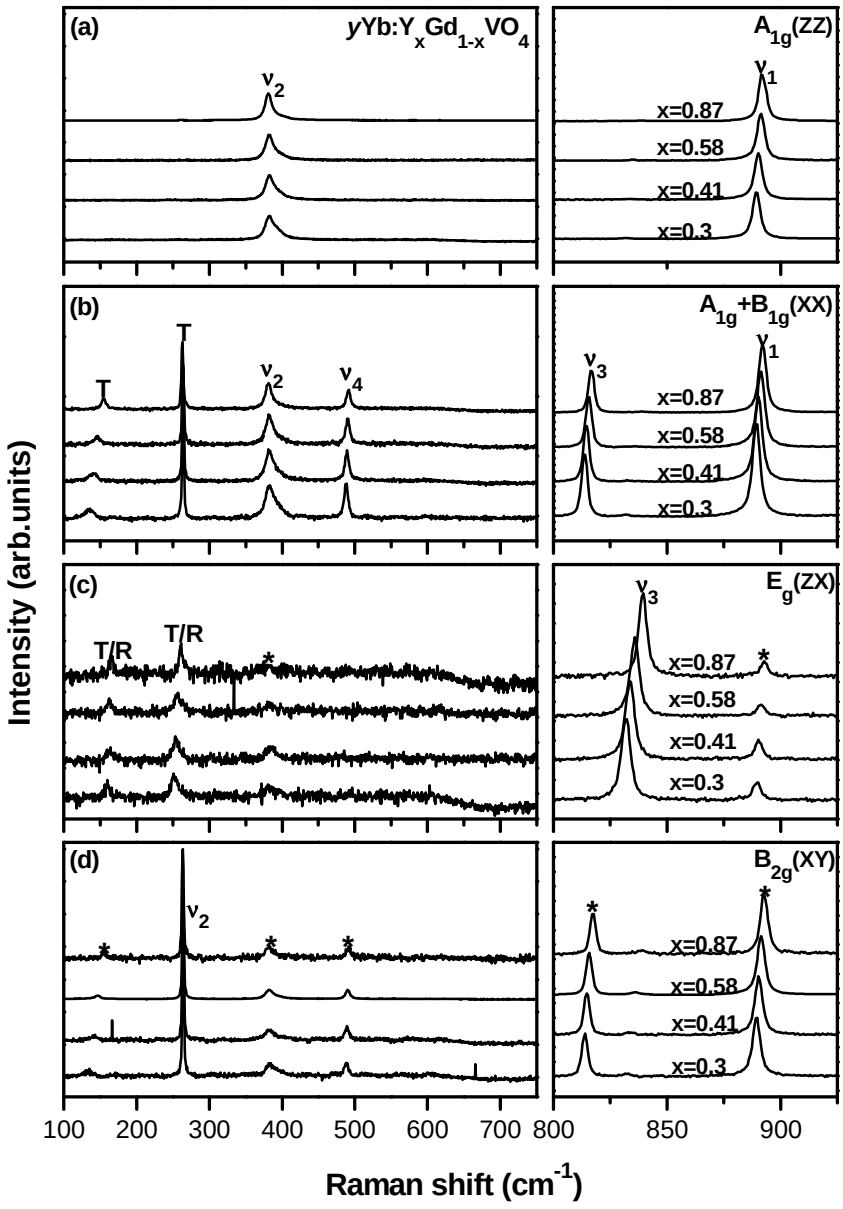

Figure 3.7. Room temperature polarized Raman spectrum of yYb:$Y_xGd_{1-x}VO_4$, with (y,x) = (0.0048, 0.3), (0.0071, 0.41), (0.0092, 0.58), (0.0135, 0.87), (0.008, 1), recorded in different polarizations: (a) (zz), (b) (xx), (c) (zx) and (d) (xy)

3.3.3 One-phonon-model

In Ref. [45], Santos *et al.* investigated the phonon behavior across the series $REVO_4$ (RE = La,…,Lu) and observed that the wavenumber of the internal VO_4 phonons increased with increasing *Z*. In this case, the RE-O distance decreases which leads to an increase in the energy of the VO_4 tetrahedron resulting in the "hardening" of the internal VO_4 wavenumbers. Two out of the four external phonons also follow the trend of increasing wavenumbers as *Z* increases. This effect is related to the overall lattice contraction (~18%) when RE goes from La to Lu. On the other hand, the two B_{1g} modes exhibit different behaviors: while the wavenumber of the mode at 260 cm^{-1} remains practically constant, the wavenumber of the mode at 120 cm^{-1} tends to decrease across the series.

To explain the behavior of the high- and low-wavenumber B_{1g} lattice modes, they considered that those modes correspond, respectively, to an *out-of-phase* and an *in-phase* movements of the RE and VO_4 units, which alternate along the [001] direction forming linear chains (see Figs. 3 (a) and 3 (b) of Ref. [45]). These normal modes roughly correspond to the longitudinal acoustic (lower wavenumber) and optical (higher wavenumber) modes. Near to the center of the one-dimensional Brillouin zone, the wavenumbers would be given by $\omega_{\text{out-of-phase}} \propto \sqrt{1/\mu}$, where $1/\mu = 1/m_{\text{RE}} + 1/m_{\text{VO}_4}$ is the reduced mass of the RE–VO_4 system, and $\omega_{\text{in-phase}} \propto \sqrt{1/(m_{\text{RE}} + m_{\text{VO}_4})}$, i.e., it depends on the mass of the RE–VO_4 chain. Therefore, when RE proceeds from La to Lu, the $\omega_{\text{out-of-phase}}$ is dominated by m_{VO4}, since $m_{\text{VO4}} < m_{\text{RE}}$. This explains why the wavenumber of the high-frequency B_{1g} mode remains practically constant across the series. On the other hand, as m_{RE} increases, $\omega_{\text{in-phase}}$ decreases as observed.

When Y replaces for Gd, the expression for $\omega_{\text{out-of-phase}}$ predicts an increase of ~17% in the wavenumber of the high-wavenumber B_{1g} mode, which is not observed. However, the expression for $\omega_{\text{in-phase}}$ predicts an increase (~10%) in the wavenumber of the low-

wavenumber B_{1g} mode. Since Y and Gd shares the same symmetry site D_{2d}, the expression for $\omega_{\text{in-phase}}$ now reads:

$$\omega_{\text{in-phase}} \propto \sqrt{1/\left((1-x)\,m_{\text{Gd}} + x\,m_{Y} + m_{\text{VO}_4}\right)}\,. \qquad (1)$$

Normalizing by $\omega^{Gd}_{\text{in-phase}}$ in order to eliminate the constant of proportionality, and considering the relation $\dfrac{1}{1-u} \approx 1+u\ (u<1)$, we obtain:

$$\left(\frac{\omega^{x}_{\text{in-phase}}}{\omega^{Gd}_{\text{in-phase}}}\right)^2 = \frac{1}{1-\left(\dfrac{m_{\text{Gd}}-m_{Y}}{m_{\text{Gd}}+m_{\text{VO}_4}}\right)x} \approx 1+\left(\frac{m_{\text{Gd}}-m_{Y}}{m_{\text{Gd}}+m_{\text{VO}_4}}\right)x\,. \qquad (2)$$

In Fig. 3.8 we plotted $\left(\omega^{x}_{\text{in-phase}}/\omega^{Gd}_{\text{in-phase}}\right)^2$ for all the compounds listed in Table 3.1. They exhibit a linear behavior described by $y = 0.65(1)x + 0.986(7)$. Even though that the slope is larger than the predicted one (~ 0.25), the one-phonon-model provides a good description of the observed behavior. The deviation from the experimental results is certainly related to the simplicity of that model.

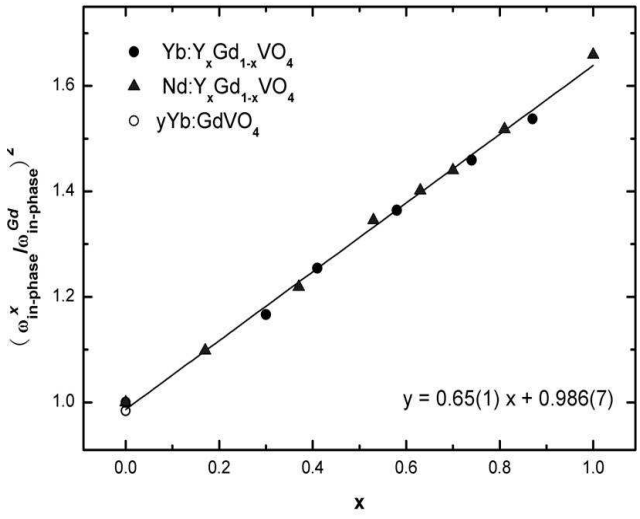

Figure 3.8. Plot of $\left(\omega^{x}_{\text{in-phase}}/\omega^{Gd}_{\text{in-phase}}\right)^2$ for all the compounds listed in Table 3.1. The straight line is the fit using Eq.(2)

3.4 Conclusion

In this chapter Raman scattering study of mixed (Nd,Yb):$Y_xGd_{1-x}(VO_4)$ crystals at room temperature were investigated what changes occured in the Raman spectrum when Nd, Yb and Y are added to $GdVO_4$. The phonon symmetry assignments were given and the observed wavenumbers were correlated with x to establish systematic variations. For Yb:$GdVO_4$, neither broadening nor wavenumber shifting of the modes were observed, indicating that Yb doping up to 0.035 produces no significant modification of the $GdVO_4$ structure. For Nd:$Y_xGd_{1-x}(VO_4)$ and *y*Yb:$Y_xGd_{1-x}(VO_4)$ we observed that the wavenumber of most of the modes increase with increasing x; irrespective of Nd and Yb levels considered. This one-phonon-like behavior is due to the lattice contraction when Gd is replaced by Y.

4

CALCIUM BARIUM NIOBATE (CBN) CRYSTALS

4.1 Introduction

Here we used Raman spectroscopy to record the room temperature phonons of alkali metal doped KNCBN ($K_{0.12}Na_{0.08}Ca_{0.28}Ba_{0.62}Nb_2O_6$) and NCBN ($Na_{0.048}Ca_{0.26}Ba_{0.716}Nb_2O_6$), and pure CBN26 and CBN32 crystals. The ferroelectric phase transition points of CBN-like crystals were obtained from DSC measurements, the higher-temperature Raman spectra of CBN32 was recorded to verify this phase transition, and the low-temperature Raman spectra of CBN32 crystal was also recorded to investigate the crystal stability.

4.2 Experimental procedure

4.2.1 Crystal growth

The crystals were grown by Wenlan Gao, Huaijin Zhang, Jiyang Wang, *et al*. in the State Key Laboratory of Crystal Materials of Shandong University (China).

(1) The crystal growth apparatus

As described in Ref [55], the CBN single crystals were grown by the Czochraski method in the DJL-400 pulling apparatus, the temperature control was achieved by a

EUROTHERM2604 with precision of ± 0.1 °C, and the craw distance of the pulling apparatus was less than 1 μm.

(2) The synthesis of polycrystalline material

The raw materials used for the synthesis of CBN polycrystalline materials were $CaCO_3$, $BaCO_3$, Na_2CO_3, K_2CO_3, Nd_2O_3 and Nb_2O_5 with 99.99% purity. The weighted amounts were combined together with the appropriate molar proportion, and then the mixture was grinded, mixed and heated at 1000 °C for 12 h in a platinum crucible. After the crucible cooled down to room temperature, the mixture was pressed into pellets and reheated at 1100 °C for 12 h.

(3) Crystal growth

The synthesized polycrystalline materials were placed in an iridium crucible with 66 mm in diameter and 40 mm in height, and were melted by an intermediate-frequency heater. A *c*-axis SBN rod of 3 mm in diameter and 20 mm in length was used as a seed. The growing atmosphere was in nitrogen containing 2 % oxygen by volume. The pulling rate varied from 1 to 3 mm/h, the crystal rotation rate was kept between 8 and 15 rpm. After reaching an ideal diameter, the pulling rate was set at 1-2 mm/h, and a rotation rate 5-20 rpm. Finally, the crystals were cooled to room temperature at a rate of 15 °C/h.

(4) Annealed process

The as-grown crystals were annealed by the following procedure: firstly, they were placed in the isothermal zone of the annealing furnace, and then heated slowly to 1100 °C at a rate of 22 °C/h in air and maintained at this temperature for 36 h, finally, they were cooled down to the room temperature at a rate of 20 °C/h.

The morphology of as-grown CBN crystals is shown in Fig 4.1.

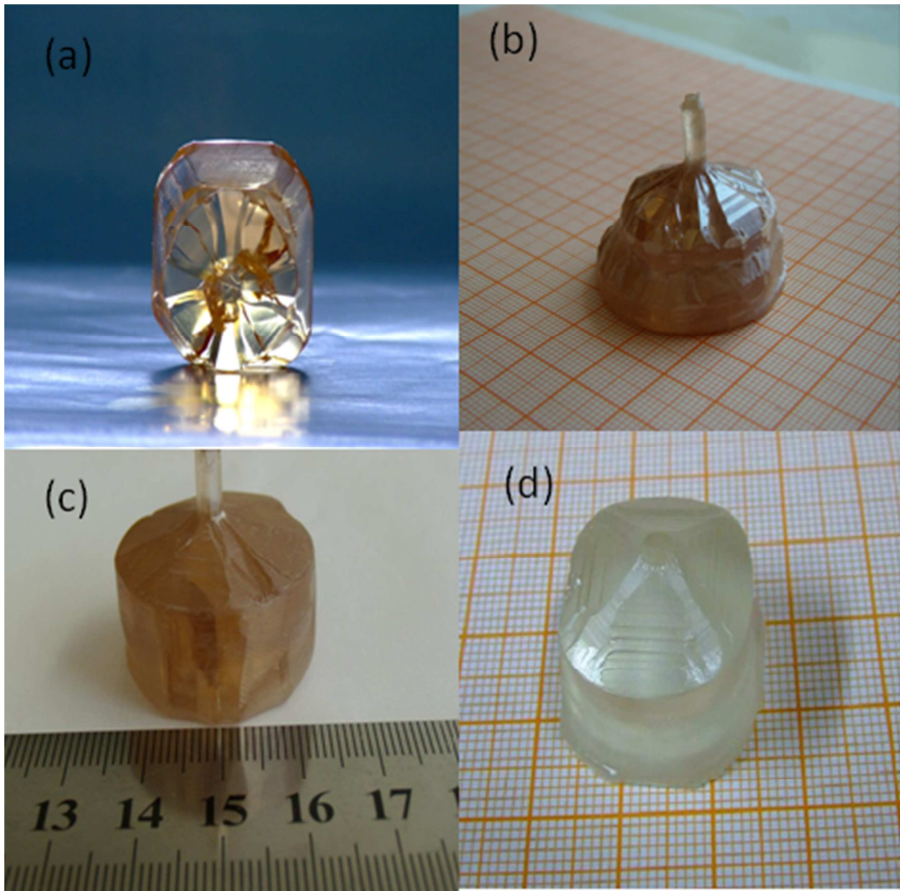

Figure 4.1. The morphology of as-grown CBN crystals. (a) CBN26 (b) CBN32 (c) NCBN (d) KNCBN

4.2.2 Characterizations

(1) X-ray four-circle diffraction experiment

The room temperature single-crystal X-ray data were collected on a CCD diffractometer (Broker Smart ApEx II) with a graphite monochromatic MoK_{α} radiation (λ = 0.71073 Å). The structure was solved by direct methods and refined using a full-matrix least-squares calculation (SHELXTL-97 program [51]).

(2) Specific heat

The specific heat measurements were performed on heating at a rate of 10 K/min using a differential scanning calorimeter (Diamond DSC).

(3) Raman spectra

We used the same setup described in Chapter 2. The typical crystals selected for the Raman study consisted of parallelepipeds, whose average dimensions were 5 × 6 × 7 mm^3. For temperature measurements we used a Linkam THMS600 stage and a T95-LinkPad system controller to vary the temperature in the range from 25 to 260 K (on cooling) and 298 to 568 K (on heating) with a precision of ± 0.1 ^oC.

4.3 Results and discussion

4.3.1 Crystal compositions and structure

Table 4.1 displays the nominal concentration, lattice parameters (*a* and *c*), unit cell volume (V) and Tc for the CBN crystals investigated. All the CBN crystals belong to the TTB structure (tetragonal, C_{4v}^2 and $Z = 5$). For CBN32, a = 12.4535(1) Å, c = 3.9478(1) Å, and V = 612.26(2) $Å^3$, while for CBN26, a =12.4480(1) Å, c = 3.9620(1) Å, and V = 613.92(2) $Å^3$.

Table 4.1. The nominal concentration, lattice parameters (*a* and *c*), unit cell volume (V) and T_C of CBN crystals

	Crystals	Unit cell parameters (Å)		Unit cell volume ($Å^3$)	Curie temperature (K)
		a	c	V	T_c
CBN32	$Ca_{0.32}Ba_{0.68}Nb_2O_6$	12.4535(1)	3.9478(1)	612.26(2)	458
KNCBN	$K_{0.12}Na_{0.08}Ca_{0.28}Ba_{0.62}Nb_2O_6$	12.4411(2)	3.9571(1)	612.48(2)	592
CBN26	$Ca_{0.26}Ba_{0.74}Nb_2O_6$	12.4480(1)	3.9620(1)	613.92(2)	567
NCBN	$Na_{0.048}Ca_{0.26}Ba_{0.716}Nb_2O_6$	12.4516(1)	3.9610(1)	614.12(2)	578

Some of the important parameters related to the structure refinement procedure [51] are listed in Table 4.2.

Table 4.2. The structure refinement information of CBN crystals

Crystals	CBN32	KNCBN	CBN26	NCBN
S	1.115	1.23	1.182	1.134
R1	0.0358	0.0668	0.0272	0.0528
ωR_2	0.095	0.1449	0.0635	0.141

As reported by Burianek *et al*. [53] only *c* changes significantly with composition; while *a* remains nearly constant. The increase in V results from the replacement of smaller Ca^{2+} by Ba^{2+} cations.

4.3.2 Raman spectrum

In the C_{4v} space group the atoms distributed in the 46 crystallographic sites give rise to 138 normal modes, which can be classified in terms of the following irreducible representations: $\Gamma_{tol} = 19A_1(R,IR) + 15A_2 + 14B_1(R) + 18B_2(R) + 36E(R,IR)$. The 120 Raman-active modes are: $\Gamma_R = 18A_1+14B_1+18B_2+35E$.

Previous spectroscopic studies on several crystals exhibiting TTB structure as SBN-like [58, 102-104], PBN [49] and $Ba_4Nd_2Ti_4Nb_6O_{30}$ [105] show that the Raman spectra are mainly dominated by bands related to the internal modes of the NbO_6 octahedron. The Raman-active modes of free NbO_6 octahedron with O_h symmetry is $\Gamma_{Oh} = A_{1g}(\nu_1)+E_g(\nu_2)+F_{2g}(\nu_5)$, where ν_i (i = 1, 2, 5) corresponds to the (A_{1g}, Nb-O bond), (E_g, O-Nb-O stretch vibration modes) and (F_{2g}, O-Nb-O bend vibration modes), respectively. Since in the TBB structure NbO_6 octahedrons occupy two different symmetry sites (C_1 and C_{2v}), distortions of octahedral structure is also expected.

The Raman intensity is usually written as

$$I(\nu) = I_0(\nu)[n(\nu) + 1] \quad (1)$$

where [$n(v)$+1] is the population factor, which connects the cross section $I_0(v)$ with spectral response function $I(v)$ observed experimentally, and here the $n(v)$ is given by

$$n(\nu) = (e^{h\nu / KT} - 1)^{-1} \tag{2}$$

The effect of the population factor on the Raman mode intensity is larger at lower wavenumbers and higher temperatures. To obtain the correct result we use the reduced Raman spectra, where the population factor was eliminated.

(1) Room temperature measurements

Figures 4.2 (a)-(d) show the room temperature Raman spectra of the CBN crystals for x(zz)x, x(yy)x, z(xy)z and x(yz)x polarizations, respectively. These polarizations yield the Raman modes of A_1, A_1+B_1, B_2, and E symmetry, respectively. The peaks were decomposed using Gaussian-Lorentzian functions and a homemade pc-based program. The assignment proposed is based on the previous results reported in Refs. [50, 104-107]. The observation of broad modes is related to the inherent lattice disorder. All the wavenumbers and the possible assignments of the modes are listed in Table 4.3.

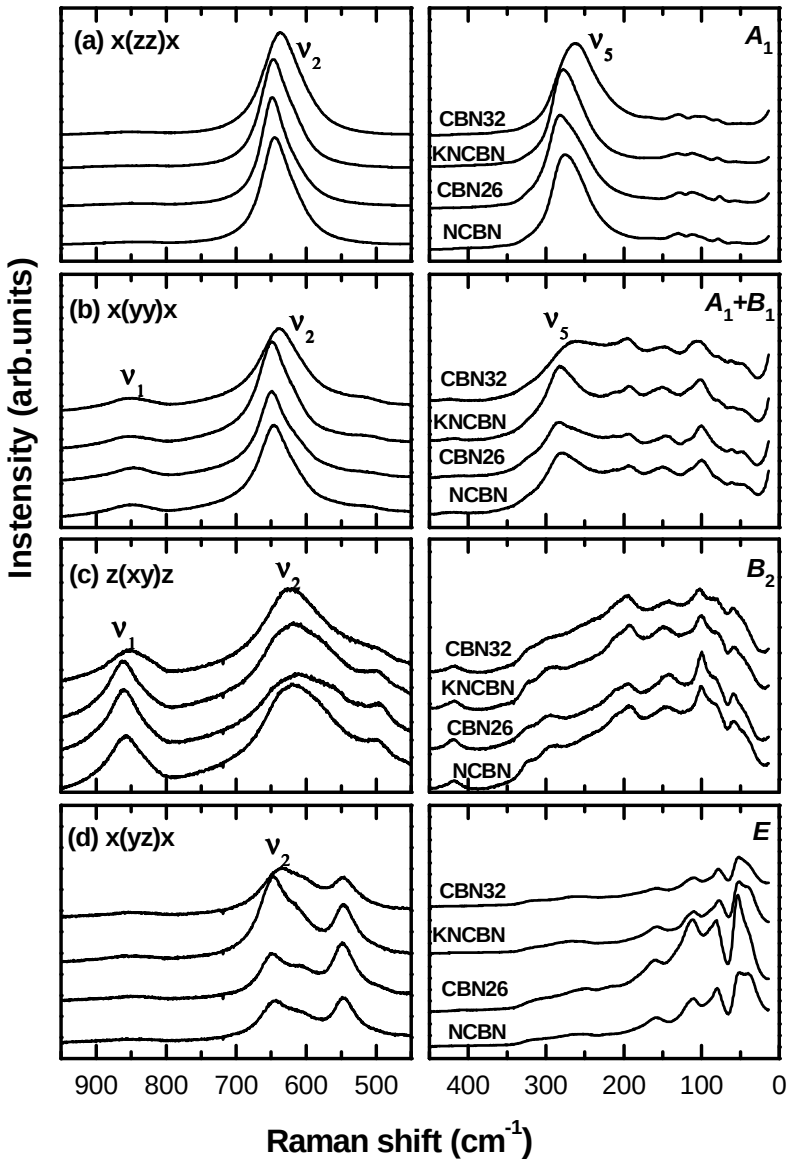

Figure 4.2. Room temperature Raman spectrum for CBN crystals recorded in different polarizations: (a)x(zz)x, (b)x(yy)x, (c)z(xy)z and (d)x(yz)x

Table 4.3. The wavenumbers (cm^{-1}) and the possible assignments of the modes observed for the CBN crystals

CBN32	KNCBN	CBN26	NCBN	Assignments	CBN32	KNCBN	CBN26	NCBN	Assignments
39	39	41	39	L(E)	166	162	162	160	L(A_1+B_1)
44	43	45	43	L(B_2)	177	162	184	172	L(E)
47	47	47	46	L(A_1+B_1)	194	192	192	192	L(A_1+B_1)
53	53	54	53	L(E)	196	192	193	193	L(B_2)
59	58	59	59	L(B_2)	220	212	217	213	L(A_1+B_1)
62	59	61	60	L(A_1+B_1)	233	214	216	219	L(B_2)
76	76	74	77	L(A_1+B_1)		248	251	252	L(B_2)
	76			L(E)	235	253	252	253	L(A_1)
78	77	79	79	L(B_2)	258	266	266	262	ν_5(A_1+B_1)
78		80	79	L(E)	263				L(B_2)
80	79	77	79	L(A_1)	266	279	282	277	ν_5(A_1)
92	90	94	92	L(E)	280	283	285	281	ν_5(A_1+B_1)
96	99	100	100	L(A_1)	294	294	295	292	ν_5(B_2)
	99		99	L(B_2)	323	325	326	325	L(B_2)
104	102	100	100	L(A_1+B_1)	423	423	420	424	L(B_2)
105		100		L(B_2)	507	500	497	504	ν_2(B_2)
	109			L(E)	546	545	547	546	ν_2(E)
109	112	112	111	L(A_1)	573	576	550	568	ν_2(B_2)
110		112	111	L(E)	606	616	608	608	ν_2(E)
		129		L(A_1)	630	631	615	624	ν_2(B)
124	120	131	123	L(E)	635	643	645	642	ν_2(A_1)
130	133		130	L(A_1)	637	647	646	644	ν_2(A_1+B_1)
141	148	134	145	L(B_2)	642	650	649	647	ν_2(E)
143	148	145	147	L(A_1+B_1)	854	862	862	859	ν_1(B_2)
158	158	160	158	L(E)	855	855	852	853	ν_1(A_1+B_1)
163		162		L(B_2)	861	859	857	872	ν_1(E)

Consider the spectra of CBN32. In Fig. 4.2 (a) we observe phonons with A_1 (z) symmetry, with polarization along the z-axis. In the low-wavenumber region (ν < 200 cm^{-1}) we observed 4 modes at 80, 96, 109 and 130 cm^{-1}. In the region 200 < ν < 450 cm^{-1} we observed an intense band assigned as ν_5(A_1). In fact, this band is composed by two bands at 235 and 266 cm^{-1}, corresponding to the vibrations at C_1 and C_{2v} symmetry sites, respectively. In the high-wavenumber region (ν > 450 cm^{-1}) we observed an intense mode at 635 cm^{-1} corresponding to the ν_2 vibration; no mode splitting is observed. The ν_1 vibration at around 850 cm^{-1} is missing. Figure 4.2 (b) shows the Raman spectra with A_1+B_1 symmetry; phonons with B_1 symmetry have no polarization. The modes observed broaden owing to the lattice disorder, and in the region ν < 450 cm^{-1}, the modes appear overlapped forming an extended band. We observed 10 vibrations in the range 40 to 300 cm^{-1}. Besides the ν_2 mode at 637 cm^{-1}, the ν_1 mode is now observed at 855 cm^{-1}. Figure 4.2 (c) shows 16 non-polar phonons with B_2

symmetry in the range 40 to 860 cm^{-1}. In Fig. 4.2 (d) we show the polar modes with *E* symmetry, which are polarized perpendicular to the *z*-axis. Twelve modes are observed. Similar phonon distribution is observed for KNCBN, CBN26 and NCBN.

The wavenumber of the external modes does not change, while the wavenumber of the internal modes shifts to higher values (blue shift) when one proceeds from CBN32 to NCBN. Usually, the blue shift is due to the lattice contraction which decreases the bond distances. However, as shown in Table 4.1, V increases (0.3%) when one proceeds from CBN32 to NCBN.

The wavenumber of the $\nu_1(B_2)$ mode increases 5 cm^{-1} from CBN32 to NCBN. According to Fig.1 of Ref. [46], the ν_1 vibration at C_1 symmetry site is related to the motion of Nb(1) and O(5) atoms, while the ν_1 vibration at C_{2v} symmetry site is related to the motion of Nb(2) and O(4) atoms, as shown in Fig. 4.3. Table 4.4 displays these relative bond distances of the CBN compounds. The shortest Nb(1)-O(5) and Nb(2)-O(4) distances at different sites decrease with increasing V. These results may indicate that the blue shift of the internal modes is likely to be related to the shortening of the Nb-O band lengths.

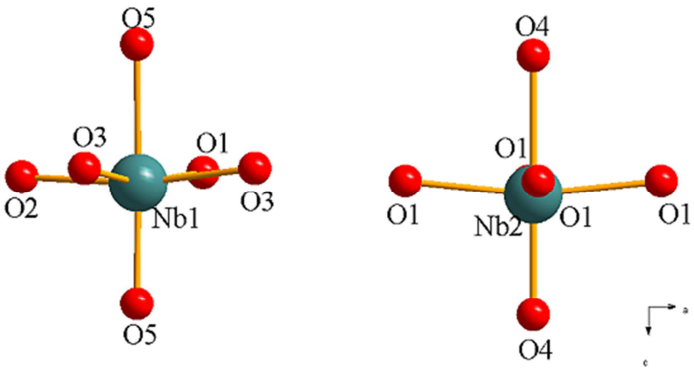

Figure 4.3. The structure diagram of octahedrons (NbO_6) of CBN crystals

(2) High- temperature measurements

Figure 4.4 shows the temperature dependence of the specific heat for all the CBN-like crystals. For CBN32, the ferroelectric to paraelectric phase transition (T_C) is observed at around 458 K, which increases to 567 K for CBN26. This shift has been previously observed by Muehlberg *et al*. [50] in CSBN crystals.

Table 4.4. The bond distances of CBN crystals

	CBN-32	KNCBN	CBN-26	NCBN
Atoms		Distances(Å)		
Nb1—O5	1.84(1)	1.814(12)	1.821(7)	1.828(10)
Nb1—O5	2.118(10)	2.151(12)	2.145(7)	2.136(10)
Nb2—O4	1.836(19)	1.82(2)	1.817(15)	1.804(19)
Nb2—O4	2.111(19)	2.13(2)	2.145(15)	2.157(19)

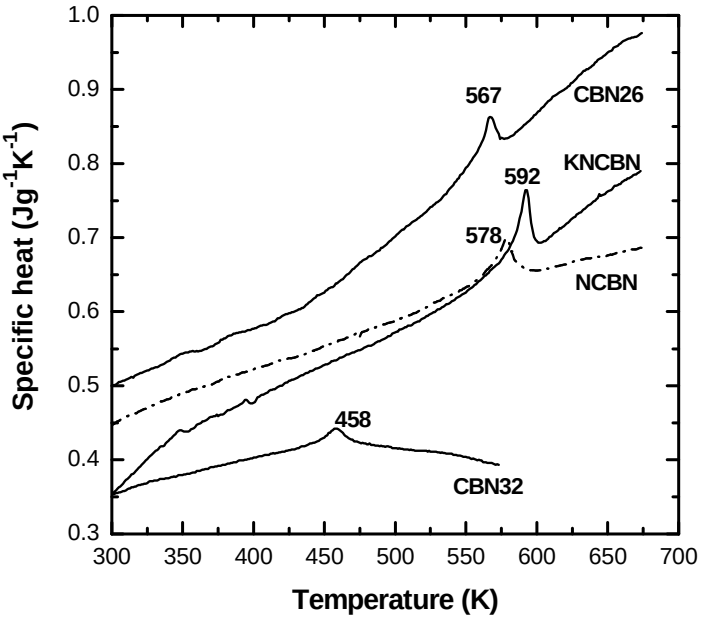

Figure 4.4. Specific heat variation of CBN-like crystals

The analysis of the temperature-dependent Raman spectra can also be used to determine T_C. In Ref. [59], Speghini *et al*. investigated T_C in the system $Sr_xBa_{1-x}Nb_2O_6$ by analyzing the thermal evolution of the wavenumber (ν) and bandwidth (FWHM) of the ν_2 vibration with A_1 symmetry. The ferroelectric characteristic of the phase transition is due to the displacement of atoms along the ferroelectric *z*-axis. For TTB structure, the transverse A_1 symmetry modes are related to the ionic motions along the *z*-axis. Thus, the corresponding Raman modes with A_1 symmetry should evidence the ferroelectric phase transition. They observed that the rate of thermally induced wavenumber softening ($cm^{-1}K^{-1}$) is different in the ferroelectric and paraelectric regions. It changes from 0.08 to 0 $cm^{-1}K^{-1}$ for x = 0.33, from 0.14 to 0.06 $cm^{-1}K^{-1}$ for x = 0.50, and from 0.3 to 0.13 $cm^{-1}K^{-1}$ for x = 0.61.

In Fig. 4.5 we show the thermal evolution (298 – 568 K) of the ν_2 (~ 635 cm^{-1}) and ν_5 (~ 260 cm^{-1}) phonons of CBN32 with A_1 symmetry. The spectra were corrected to the Bose-Einstein factor.

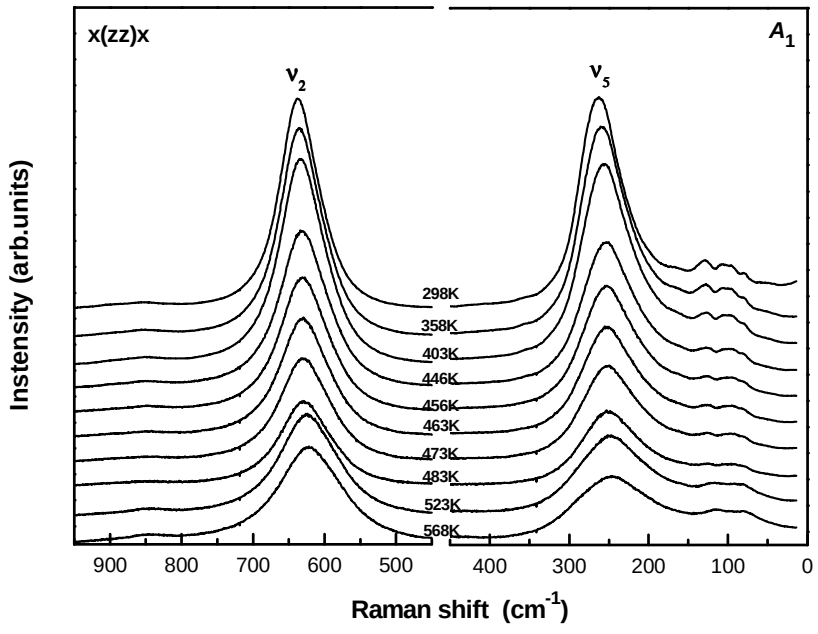

Figure 4.5. Temperature (298-568 K)-dependent Raman spectra of CBN32 in the x(zz)x geometry

In Figs. 4.6 (a) and (b) we depict the temperature dependence of ν_2 and ν_5, respectively. We observe that ν_5 decreases at a constant wavenumber softening rate with increasing T, while ν_2 also decreases as T increases but its wavenumber softening rate changes at T_C = 446 K. Therefore, information on the ferroelectric to paraelectric phase transition is obtained by analyzing the behavior of $d\nu_2/d$T.

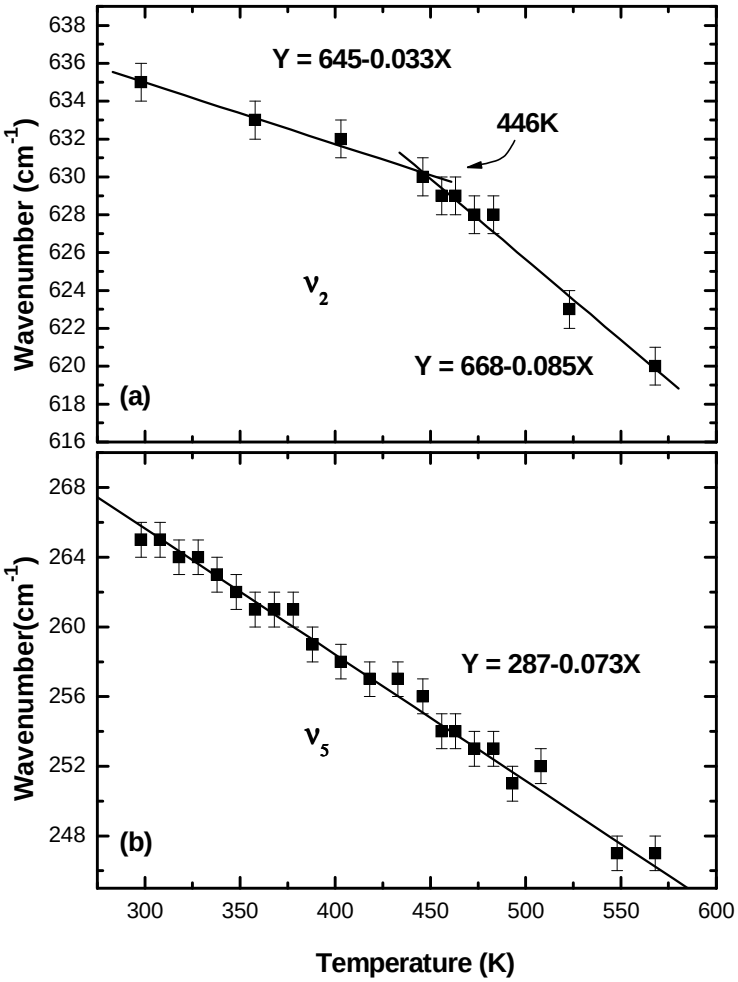

Figure 4.6. The temperature (298-568 K) dependence behavior of the wavenumbers of (a) ν_2 mode (~ 635 cm^{-1}) and (b) ν_5 mode (~ 260 cm^{-1}) of CBN32 with A_1 symmetry. The solid lines represent linear fits of the data points

The wavenumber softening rate changes from 0.033 to 0.085 $cm^{-1}K^{-1}$ as T increases. This behavior is opposite to that observed in SBN by Speghini *et al*. [59]. SBN is a relaxor ferroelectric-type crystal, whose relaxor character is related to the crystal lattice disorder. The data reported in Ref. [59] show that the relaxor character of SBN33 is smaller than that of SBN50 and SBN61. This happens because SBN33 presents a lower crystalline disorder, since it has the lowest Sr concentration. The wavenumber softening rate of CBN32 in the ferroelectric phase is smaller than that of SBN33, indicating that CBN exhibits a more normal ferroelectric character as compared with SBN, agreeing with the results of Heine *et al*.[108] using the *k*-space spectroscopy.

The fact that the wavenumber softening rate of CBN32 in the ferroelectric phase is smaller than that of paraelectric phase is likely to be related with the negative thermal expansion along the *z*-axis for T < Tc. The negative thermal expansion along the *c*-axis is attributed to the deviation of the Nb site from the center of oxygen octahedrons and the disorder in the chains along the *c*-axis that join the two types of Nb-containing octahedron. As the temperature increases, the wavenumber of phonons should shift downwards. However, owing to the negative thermal expansion, the bond distances decrease with increasing T. As a result, the wavenumber shifts upwards. The competition between these two effects surely imply in a smaller decreasing rate in the ferroelectric phase, since in the paraelectric phase the thermal expansion along the *z*-axis is positive [55].

(3) Low-temperature measurements

In Fig. 4.7 we show the Raman spectra of CBN32 at several temperatures (25-260 K) for x(zz)x scattering geometry. The unsymmetry ν_5 mode can be decomposed into higher- and lower- modes by the Gaussian-Lorentzian function.

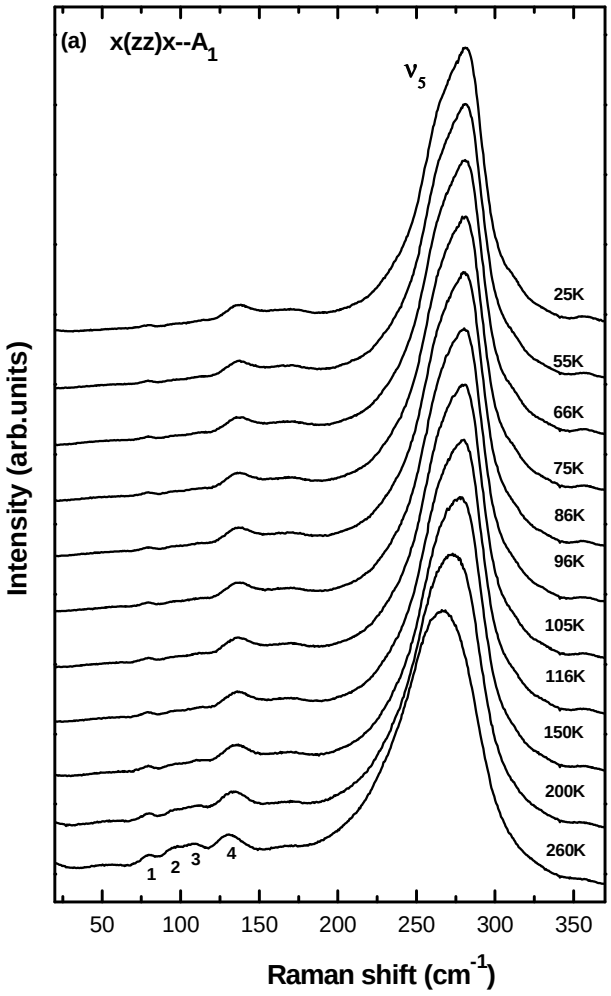

Figure 4.7. Temperature (25-260 K) -dependent Raman spectra of CBN32 in the x(zz)x geometry

The low-temperature dependence behavior of the (a) wavenumbers and (b) FWHM (cm^{-1}) of higher- and lower-ν_5 mode with A_1 symmetry is plotted in Fig.4.8, respectively. We observed that the rate of the temperature dependence behavior of both wavenumbers of lower-ν_5 mode and FWHM(cm^{-1}) of higher-ν_5 mode change abruptly at 75-100 K, which indicate that CBN32 crystal may exhibit a possible phase transformation below 100 K.

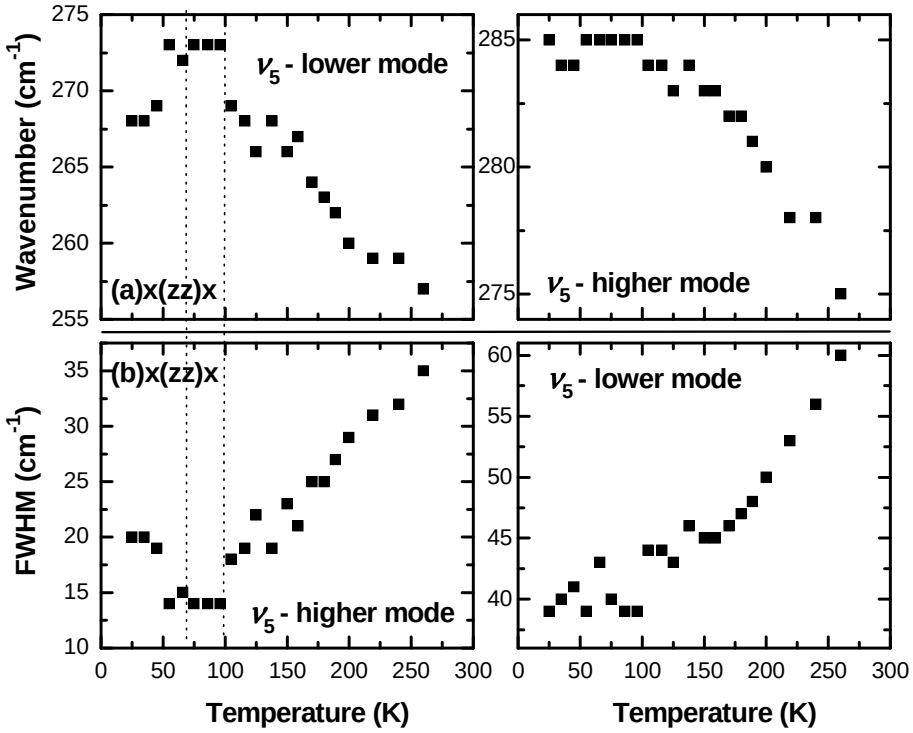

Figure 4.8. The temperature (25-260 K) dependence behavior of the (a) wavenumbers and (b) FWHM (cm^{-1}) of higher- and lower-ν_5 mode with A_1 symmetry, respectively

In some cases, the phase transition can also be identified by analyzing the relative intensity of Raman bands. For instance, Cheng *et al*. [109] analyzed the ratio intensity changes with increasing T to determine the monoclinic-tetragonal-cubic phase transition sequence in PZN-PT crystals. Similar procedure has been used by Silberman *et al*. [110] in the study of the phase transition in triglycine sulfate, and Faria *et al*. [58] in the investigation of low-temperature phase transition in SBN fiber crystal. This procedure has been shown to be fruitful in the investigation of phase transitions in relaxor-based ferroelectric materials [111-113].

Consider the bands labeled by 1, 2, 3 and 4 appearing at 260 K in Fig. 4.7, As T decreases the intensity of bands 2 (I_2) and 3 (I_3) becomes lower than that of band 4 (I_4). When

the intensity ratios I_2/I_4 and I_3/I_4 are plotted against temperature (see Fig.4.9), it is observed that for temperatures below 90 K, the increasing rate is either constant or changes slightly. However, above 90 K the slope changes appreciably. These results may indicate that CBN32 undergoes a phase transition for temperatures at around 90 K. The possible phase transformation should be related to a change in the neighborhood of one or both symmetry sites occupied by the NbO_6 octahedrons [58].

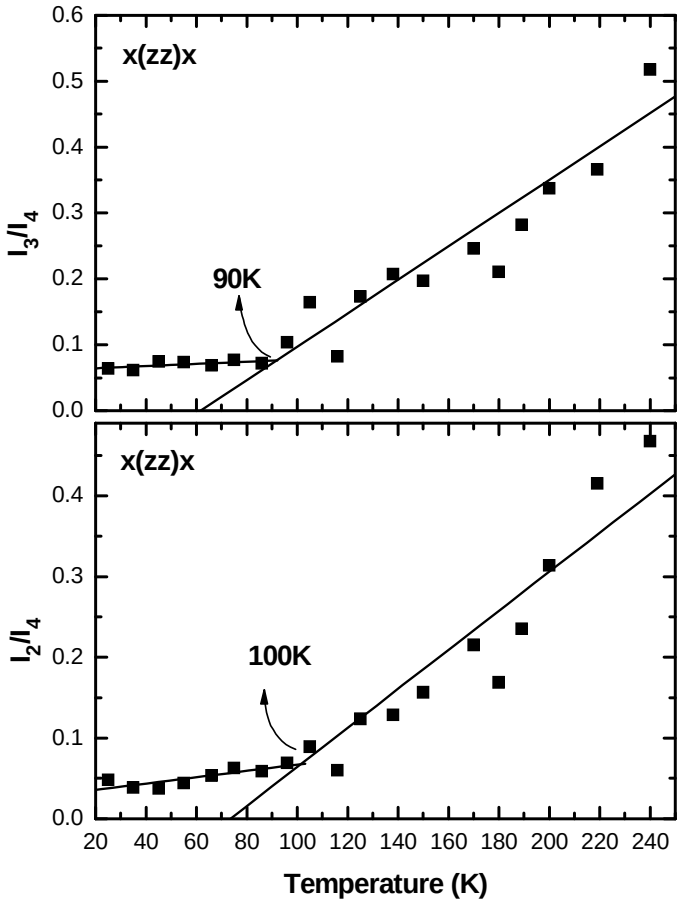

Figure 4.9. The temperature (25-260 K) dependence of the intensity ratios I_2/I_4 and I_3/I_4 of CBN32 with A_1 symmetry

4.4 Conclusion

In this chapter we carried out Raman measurements to determine the room temperature phonons of CBN32, KNCBN, CBN26 and NCBN crystals. We observed fewer and broad bands. The broadening of the bands is related to the intrinsic disorder of the TBB structure. The reason why fewer modes are observed in all the scattering geometries than formally predicted is twofold: (i) some modes have very weak polarizability derivatives leading to very weak bonds which are not seen, and (ii) the correlation field splitting may be so small that the factor group components are not completely solved. The phonon symmetry assignments were based on correlations with previous results in other CBN and SBN compounds. We observed that the wavenumbers of the internal NbO_6 phonons increase with increasing V. This wavenumber "hardening" was associated to the decrease of the Nb-O distances when one proceeds from CBN32 to NCBN.

From DSC curves we determined T_C and observed that it increases with decreasing Ca content. Temperature-dependent Raman spectra (25-568 K) of CBN32 were recorded and the changes observed were discussed. The results indicates that CBN32 undergoes the well-known ferroelectric to paraelectric phase transition at T_C = 446 K and a possible phase transformation at T = 75-100 K.

5

POTASSIUM TANTALITE NIOBATE (KTN) CRYSTALS

5.1 Introduction

Here we determined the complete sequence of phase transitions of highly-diluted KTN_x (x = 0.45, 0.50 and 0.55) single crystals by analyzing from the temperature-dependent Raman spectrum what features can represent the signature of the orthorhombic (*O*)-rhombohedral (*R*) phase transition.

5.2 Experimental procedure

5.2.1 Crystal growth

The crystals were grown by Xuping Wang, Nana Zhang, Jiyang Wang, *et al*. in the State Key Laboratory of Crystal Materials of Shandong University (China).

(1) The crystal growth apparatus

As described in Ref. [114], KTN_x single crystals (x denotes the nominal composition) with different compositions were grown by the Czochraski method in a TDL-H50AC crystal-pulling apparatus. The platinum crucible was heated using a 2 kHz intermediate frequency

heater. The temperature control apparatus was a EUROTHERM 818 controller/programmer with a precision of ± 0.3 °C, the craw distance of the pulling apparatus was less than 1 μm.

(2) The synthesis of polycrystalline KTN

Chemical regents, K_2CO_3, Ta_2O_5 and Nb_2O_5, with 99.99% purity were used as raw materials for synthesis of KTN polycrystalline. Based on the phase diagram shown in Fig 5.1,

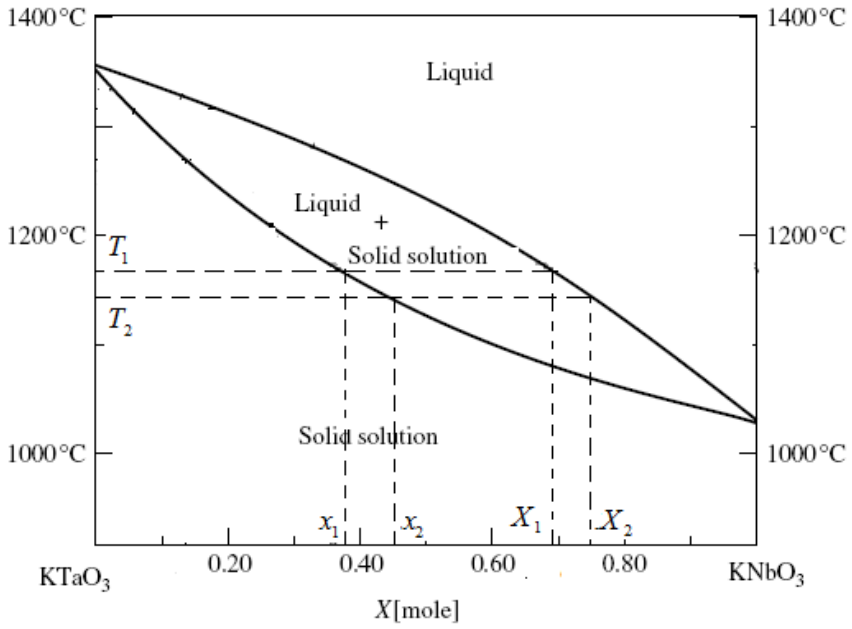

Figure 5.1. The phase diagram of KTN crystal

the raw materials were weighted out in the appropriate molar proportion as the following reaction equation (1) ,

$$K_2CO_3 + xNb_2O_5 + (1-x)Ta_2O_5 = 2KTa_{(1-x)}Nb_xO_3 + CO_2 \uparrow \qquad (1)$$

The weighted amounts were mixed well, pressed into pellets at about 10^8 Pa, and then placed into a Pt crucible and heated at about 1100 °C for 15-20 h. The raw materials reacted.

(3) Crystal growth

A rectangular cubic KTN single crystal bar with dimensions of 3 × 3 × 30 mm was used as the seed. The experiments were performed in air atmosphere. The pulling rate was kept at 0.3 – 0.5 mm/h, and the crystal was rotated at a rate of 5 – 10 rpm during growth. After the crystal diameter reached a certain value, they were cooled to the room temperature at a speed of 30 – 50 °C/h.

Due to the phase transitions, inhomogeneity and formation of growth striations, it is very difficult to obtain good quality KTN crystals, specially the crystals with higher Nb contents. Therefore, we adopted several precautions during the growth process. To reduce the variation of the proportions of the melting components, large crucibles with 80 mm (in diameter) × 60 mm (in height) and 150 mm (in diameter) × 100 mm (in height) were used to grow a small sized 50 g KTN crystals. It is also very important to grow the crystal at a relatively constant temperature.

We grew a series of KTN crystals as shown in Fig 5.2, whose specific compositions and sizes are listed in Table 5.1. The upper part of pure KT crystal (sample (I)) is opaque due to vacancy or the inclusion defects resulting from the faster crystal growth rate. The KTN45 (sample (IX)) is also opaque, owing to the cubic-to-tetragonal phase change occurring at room temperature where domain defects are formed. The remaining samples are colorless and transparent.

Table 5.1. The specific information of as-grown KTN crystals

No.	*formula*	*x*	*Size (mm)*
I	$KTaO_3$	0	35×33×50
II	$KTa_{0.91}Nb_{0.09}O_3$	0.09	27×27×15
III	$KTa_{0.86}Nb_{0.14}O_3$	0.14	10×8×20
IV	$KTa_{0.81}Nb_{0.19}O_3$	0.19	12×13×15
V	$KTa_{0.75}Nb_{0.25}O_3$	0.25	18×18×24
VI	$KTa_{0.67}Nb_{0.33}O_3$	0.33	20×20×30
VII	$KTa_{0.65}Nb_{0.35}O_3$	0.35	15×15×20
VIII	$KTa_{0.63}Nb_{0.37}O_3$	0.37	10×12×13
IX	$KTa_{0.55}Nb_{0.45}O_3$	0.45	20×20×50

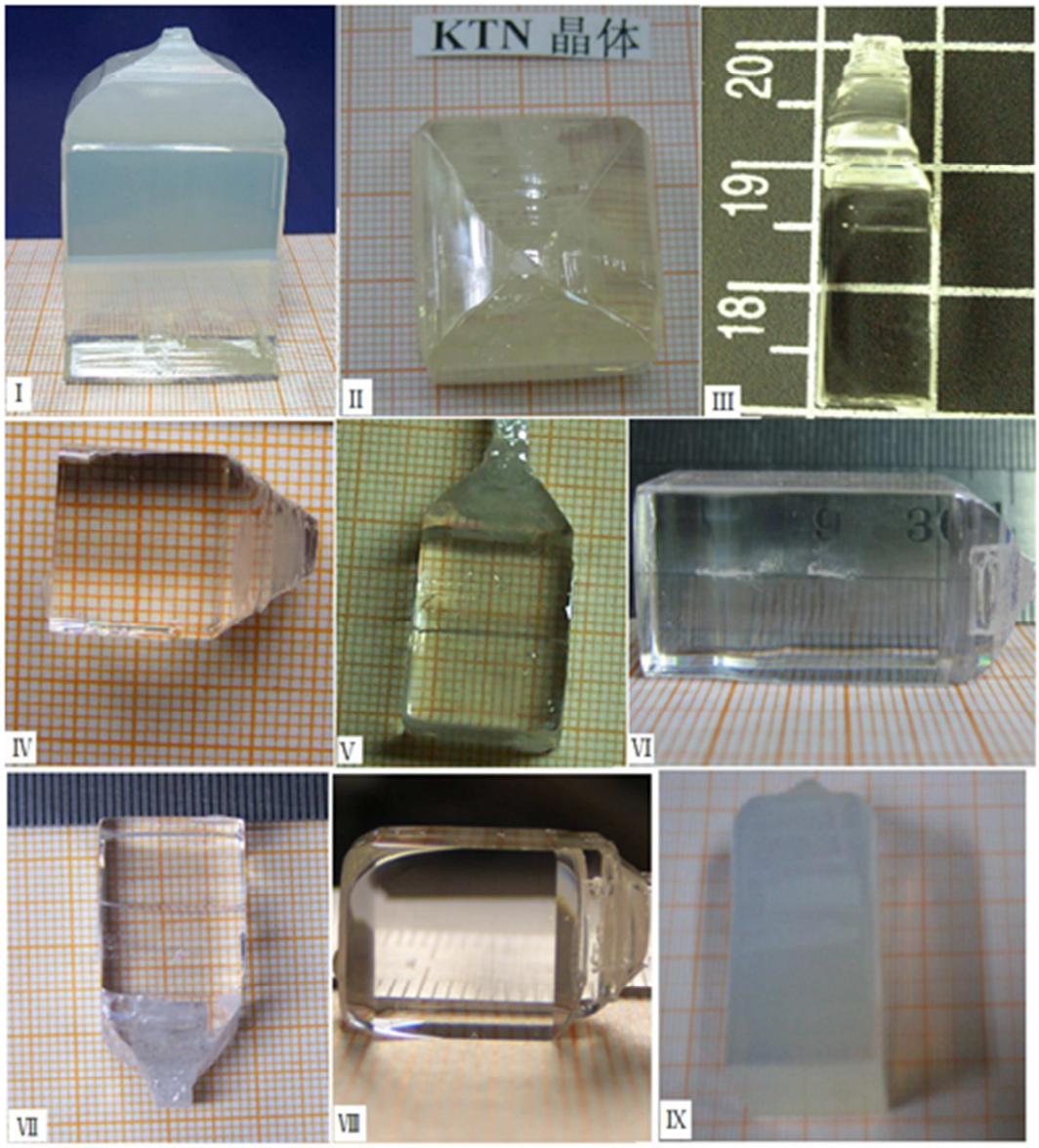

Figure 5.2. The morphology of as-grown KTN crystals

5.2.2 Characterizations

Temperature dependent backscattered Raman spectra at several temperatures were recorded on a Jobin-Yvon Model T64000 triple spectrometer with a spectral resolution of 2 cm^{-1}. The instrument was equipped with a liquid-N_2-cooled charge-coupled device system. For spectral excitation, green 514.5 nm radiation from a Coherent Model Innova 70 Ar^+-ion

laser operating at 30 mW was employed. We used a Linkam THMS600 stage and a T95-LinkPad system controller to vary the temperature in the range from 600 to -196 ^{o}C with a precision of ± 0.1 ^{o}C. All measurements were performed on cooling.

5.3 Results and discussion

5.3.1 Crystal structure and Raman-active modes

(1) Crystal structure

KTN crystal is a well studied solid solution with ABO_3 perovskite lattice structure, as shown in Fig 5.3, where Ta and Nb ions interchange in the centers, K ions occupy the corners, and oxygen ions are placed on the faces of the cubic cells. When the temperature is sufficiently high, the KTN crystal is paraelectric with cubic ($Pm3m$, O_h^1) lattice symmetry, with cooing down, it undergoes a sequence of ferroelectric phase transitions to tetragonal lattice symmetry ($P4mm$, C_{4v}^1), to orthorhombic lattice symmetry ($Amm2$, C_{2v}^{14}) and finally to rhombohedral lattice symmetry ($R3m$, C_{3v}^5).

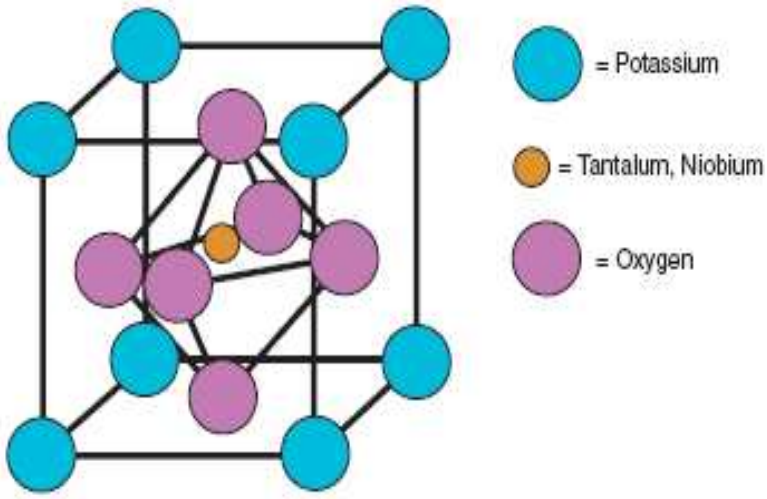

Figure 5.3. The unit-cell structure of KTN crystal

(2) Raman-active modes

KTN crystal exhibits the following sequence of phase transitions on heating: rhombohedral (R) → orthorhombic (O) → tetragonal (T) → cubic (C):

For cubic (C) phase ($Pm3m$, O_h^1) the vibration modes can be expressed as $\Gamma_{vib}= 3F_{1u}(T_x, T_y, T_z)+F_{2u}$. Here, in the ideal cubic structure, all the zero wavevector phonons are of odd parity, so it exhibits no active first-order Raman phonon.

For tetragonal (T) phase ($P4mm$, C_{4v}^1) the vibration modes can be expressed as $\Gamma_{vib} = 3A_1(T_z,\alpha_{xx}+\alpha_{yy},\alpha_{zz})+B_1(\alpha_{xx}-\alpha_{yy})+4E(T_x, T_y,\alpha_{xy},\alpha_{yz})$, where A_1 and E modes are both Raman and IR-active polar modes, and the nonpolar B_1 mode is only Raman-active.

For orthorhombic (O) phase ($Amm2$, C_{2v}^{14}) the vibration modes are $\Gamma_{vib} = 4A_1(T_z,\alpha_{xx},\alpha_{yy},\alpha_{zz})+A_2(\alpha_{xy})+4B_1(T_x, \alpha_{xz}) + 3B_2 (T_y, \alpha_{yz})$, and all are Raman-active.

For the rhombohedral (R) phase ($R3m$, C_{3v}^5) the vibration modes are distributed according to $\Gamma_{vib} = 3A_1(T_z,\alpha_{xx}+\alpha_{yy},\alpha_{zz})+A_2+4E(T_x, T_y,\alpha_{xx}-\alpha_{yy}, \alpha_{xy}, \alpha_{xz},\alpha_{yz})$, where A_1 and E mode are both Raman- and IR-active, and A_2 mode is neither Raman- nor IR-active.

5.3.2 Raman spectrum

(1) Room temperature measurements

Figures 5.4 (a)-(c) show the Raman spectrum of A_1 phonons of $KTN_{0.55}$, $KTN_{0.50}$ and $KTN_{0.45}$, respectively. They exhibit a tetragonal phase belonging to the $P4mm$ (C_{4v}^1) space group.

The modes at 875 and 556 cm^{-1} as well as the structure (resonance-depth) at 200 cm^{-1} are assigned to ν_1, ν_2 and ν_5 internal vibrations of the $(Nb,Ta)O_6$ group, respectively[67] (The

resonance-depth is related to the Fano antiresonance [115, 116]). The spectra are similar to those of $KTa_{0.5}Nb_{0.5}O_3$ deposited on MgO and $LaAlO_3$ substrates [70].

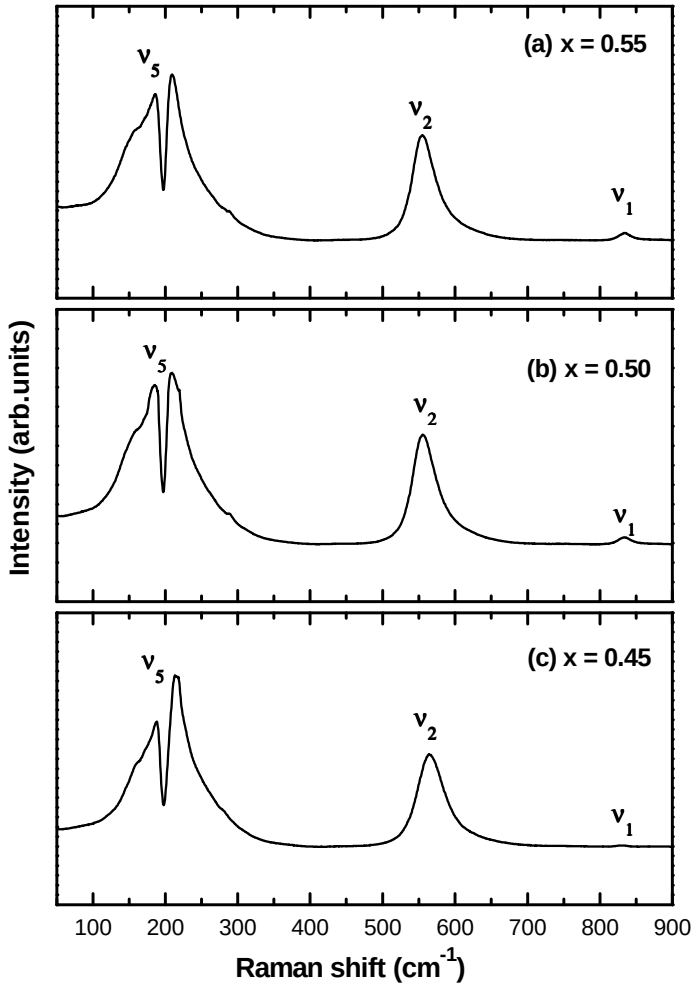

Figure 5.4. The room temperature Raman spectra of (a) $KTN_{0.55}$, (b) $KTN_{0.50}$ and (c) $KTN_{0.45}$

(2) Temperature-dependent measurements

The changes of the Raman spectrum across the different phases of (a) $KTN_{0.55}$, (b) $KTN_{0.50}$ and (c) $KTN_{0.45}$ are plotted in Figs 5.5 (a-c), respectively.

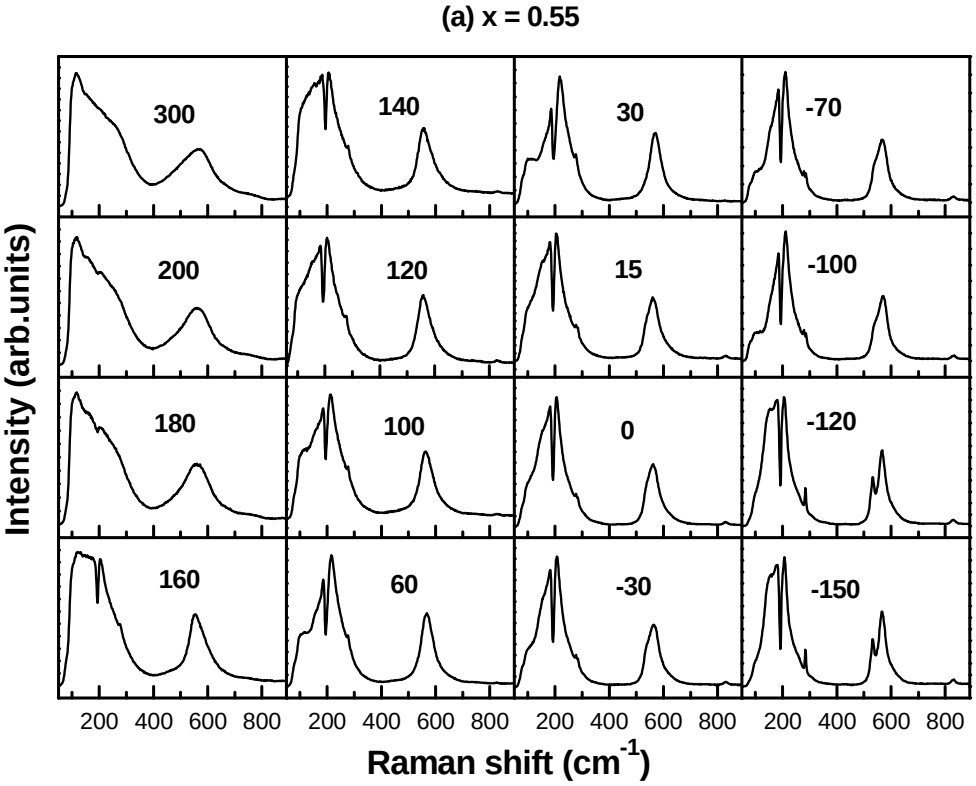
(a) x = 0.55
300
140
30
-70
200
120
15
-100
180
100
0
-120
160
60
-30
-150
Intensity (arb.units)
200 400 600 800
Raman shift (cm-1)

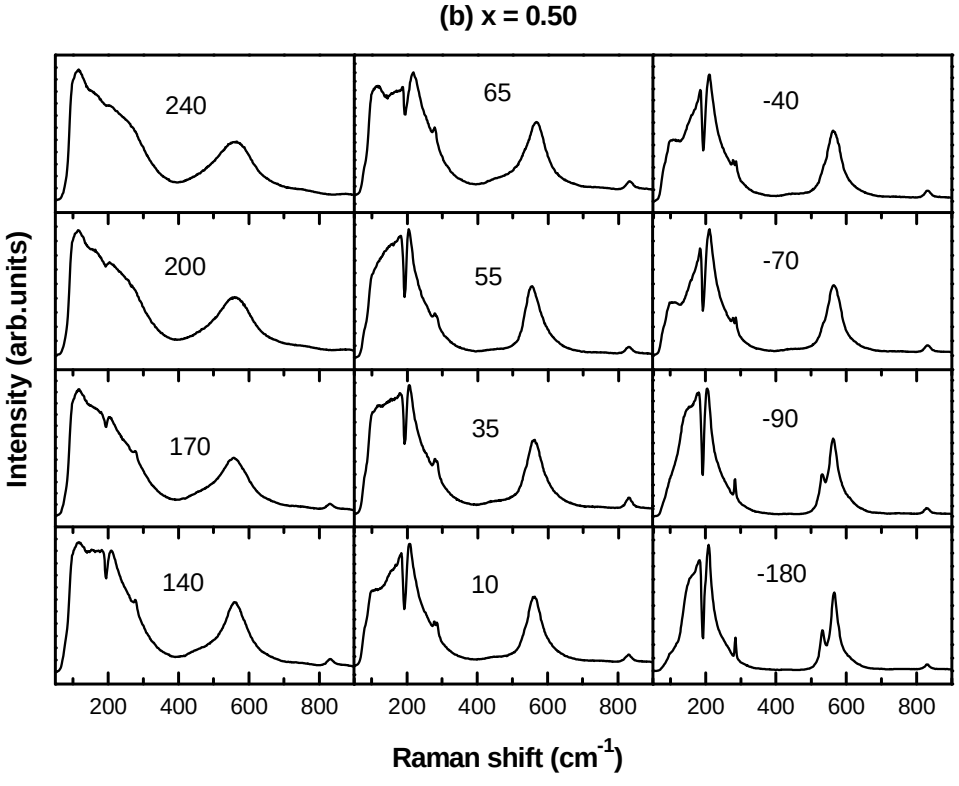
(b) x = 0.50
240
65
-40
200
55
-70
170
35
-90
140
10
-180
Intensity (arb.units)
200 400 600 800
Raman shift (cm-1)

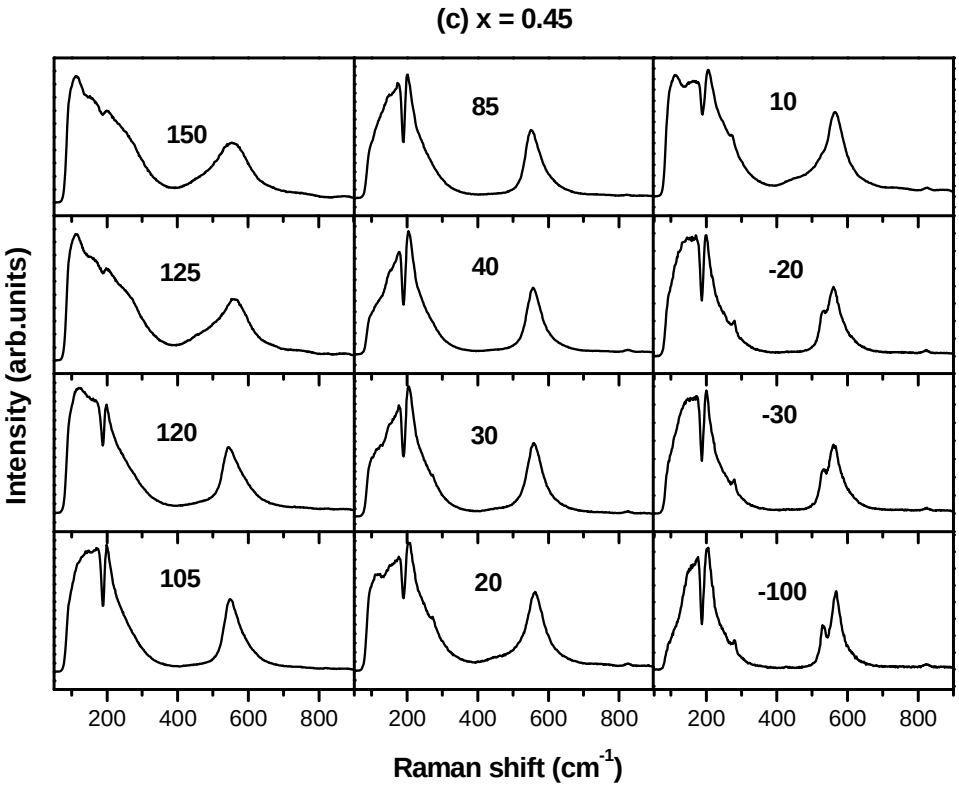

Figure 5.5. The temperature (^{o}C) evolution of the Raman spectra of (a) x = 0.55 (b) x = 0.50 and (c) x = 0.45

To better describe the phase transition points and discuss their features, we have drawn the normalized results of the temperature evolution of phonons of $KTN_{0.55}$, $KTN_{0.50}$, and $KTN_{0.45}$, show in Figs. 5.6 (a)-(c), respectively.

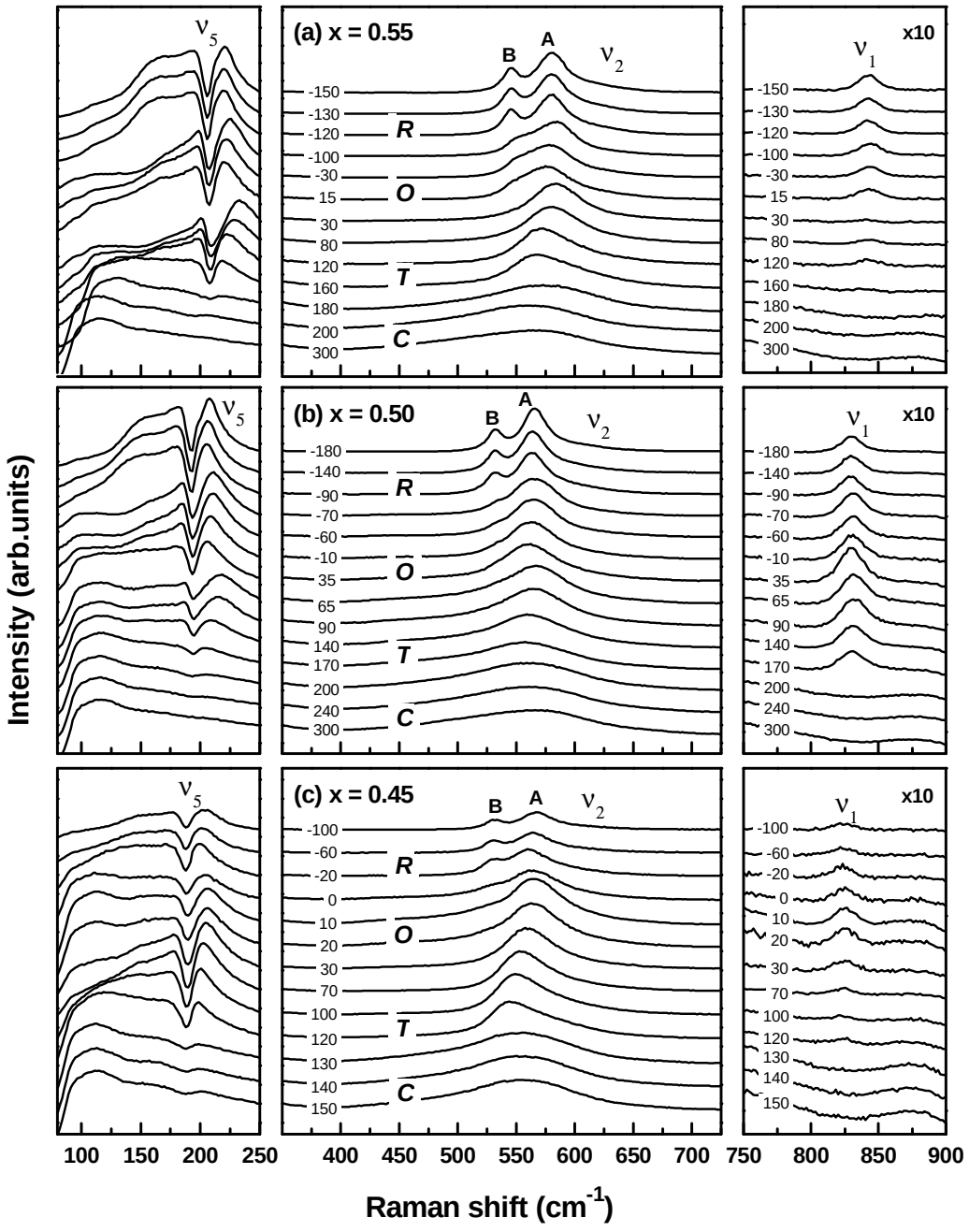

Figure 5.6. The temperature (^{o}C)-dependent Raman spectra of (a) $KTN_{0.55}$, (b) $KTN_{0.50}$ and (c) $KTN_{0.45}$

(1) *C-T* phase transition

According to Ref. [70], the *C-T* phase transition is characterized by the appearance of the ν_5 mode at around 200 cm^{-1} and a zone-center A_1 mode at around 555 cm^{-1}. By following these criteria, the *C-T* phase transition occurs at 160 ^oC, 170 ^oC, and 120 ^oC for $KTN_{0.55}$, $KTN_{0.50}$, and $KTN_{0.45}$, respectively.

(2) *T-O* phase transition

The adopted criteria to the *T-O* phase transition are changes in the ν_5 mode and the appearance of a low-frequency wing of the 560 cm^{-1} mode [66]. Let us consider the second criterion, since changes in the ν_5 mode are not clear mainly for $KTN_{0.45}$.

Figures 5.7 (a)-(c) show the selected Raman spectra of $KTN_{0.55}$, $KTN_{0.50}$, and $KTN_{0.45}$, respectively. The data analysis of the spectrum shows the temperature evolution of the low-frequency wing of the 560 cm^{-1} mode. We observed that the *T-O* phase transition occurs at 15 ^oC, 35 ^oC, and 20 ^oC for $KTN_{0.55}$, $KTN_{0.50}$, and $KTN_{0.45}$, respectively.

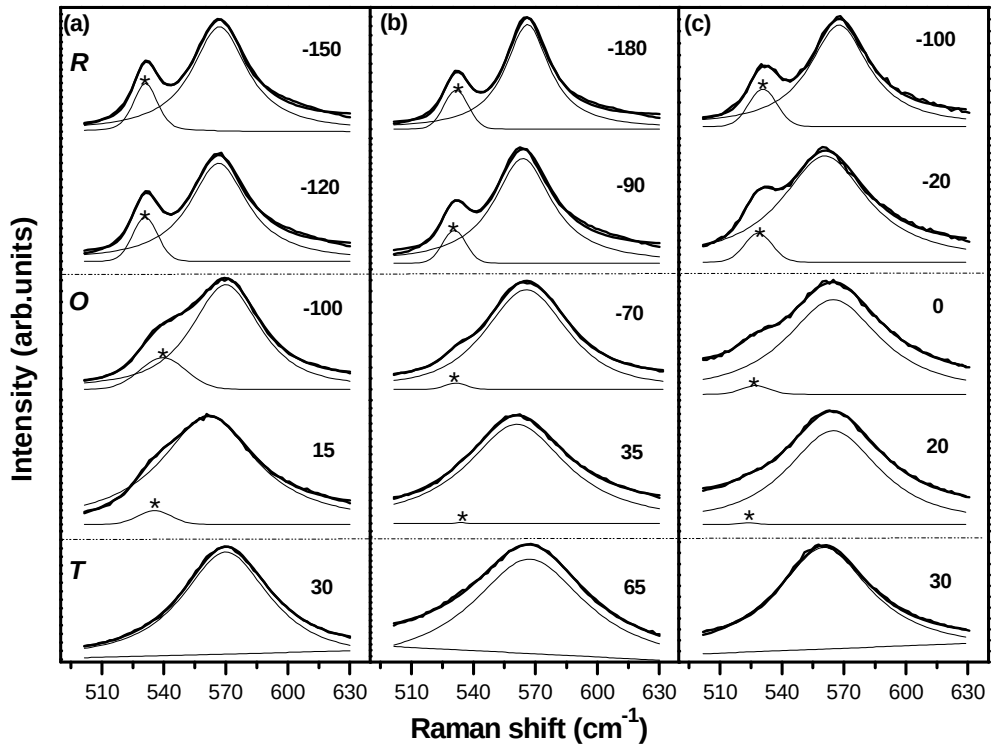

Figure 5.7. Selected Raman spectra of KTN_x and their spectral decomposition with temperature (^oC) (a) $KTN_{0.55}$, (b) $KTN_{0.50}$ and (c) $KTN_{0.45}$

(3) *O-R* phase transition

Now, let us discuss what changes in the phonon spectrum can be associated to the *O-R* phase transition. For KNO [117] and $K_{0.5+\delta}Na_{0.5-\delta}NbO_3$ (KNN) [118] compounds the *O-R* phase transition can be identified by changes in the low-frequency modes ($\nu < 250$ cm^{-1}). In these compounds well defined modes are observed, rather than the broad resonance-depth structure. Recall that Bartasyte *et al.* [70] pointed out that the changes in the phonon spectrum are expected to be observed in the 560 cm^{-1} region. Unfortunately, due to the band overlapping they did not discuss the *O-R* phase transition in the KTN/MgO and KTN/LAO thin films.

To identify the *O*-*R* phase transition in the highly-diluted KTN_x crystals, let us analyze the temperature dependence of the frequency of the Raman modes (A and B) appearing in the 500-600 cm^{-1} region plotted in Figs. 5.8 (a)-(c). Consider Fig. 5.8 (a). We observe that the slope $d\nu/dT$ of both modes changes at -120 ^oC for $KTN_{0.55}$. For $KTN_{0.50}$ and $KTN_{0.45}$ similar changes occur, and the *O*-*R* phase transition takes place at -90 and -20 ^oC, respectively.

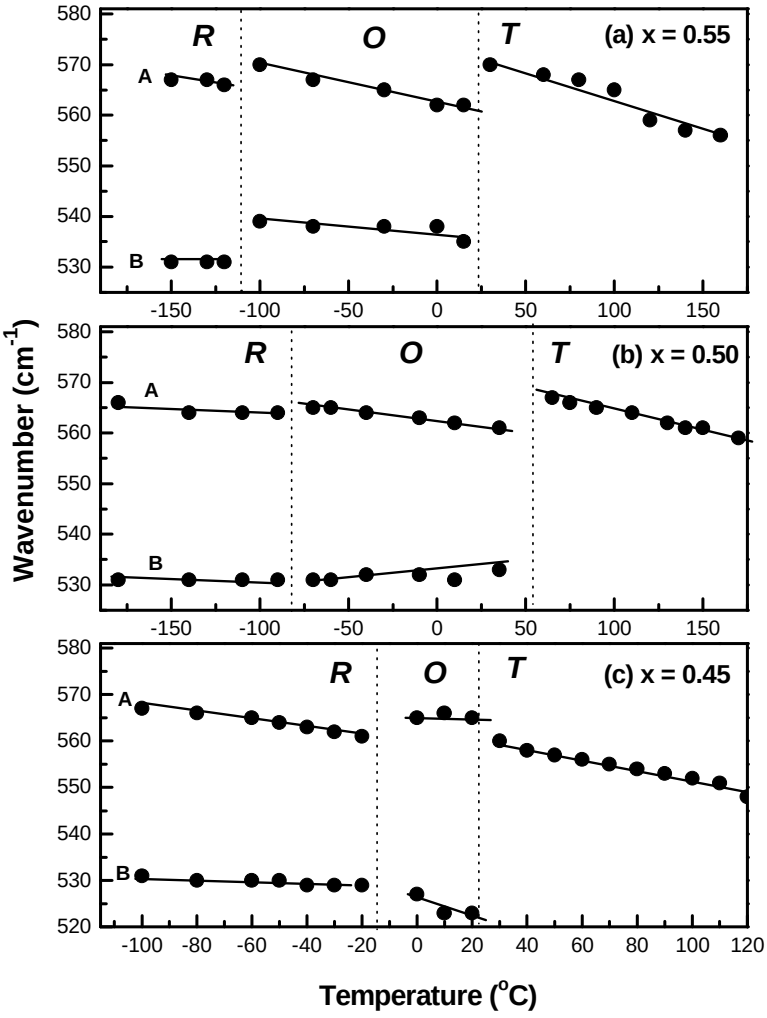

Figure 5.8. Temperature dependence of the Raman modes in (a) $KTN_{0.55}$, (b) $KTN_{0.50}$ and (c) $KTN_{0.45}$. The solid lines are guide for eyes and the dashed lines indicate the phase transition temperatures

The *O-R* phase transition can also be identified by analyzing the behavior of the relative intensity of the A and B modes of the orthorhombic phase as a function of temperature. This procedure has been used to investigate the phase transition undergone by the [(1-x)$Pb(Zn_{1/3}Nb_{2/3})O_{3-x}$ $PbTiO_3$] (PZN–PT) single crystals with x = 4.5% and 12% [49]. Above room temperature, dielectric measurements showed that both compositions exhibit structural phase transitions according to the phase diagram proposed by Kuwata *et al* [119]. Below room temperature, an anomaly at around T= -93 ^oC for the sample with x = 12% was observed, suggesting another phase transition. Raman measurements were used to study all phase transitions. Since no modification either in the number or the frequency of the vibrations evidencing the phase transitions were observed, the authors analyzed the behavior of the relative intensity of the 600 cm^{-1} (E_g) and 780 cm^{-1} (A_{1g}) bands as a function of temperature [115]. They were able to identify not only the high temperature phase transition undergone by PZN-4.5PT and PZN-12PT, but also a low-temperature phase transition undergone by PZN-12PT.

Figures 5.9 (a)-(c) show the behavior of the intensity ratio (I_A/I_B) as a function of temperature for $KTN_{0.55}$, $KTN_{0.50}$, and $KTN_{0.45}$, respectively. Here, A and B correspond to the modes at around 565 and 535 cm^{-1}, respectively. From Figs 5.9, clear changes in the behavior of I_A/I_B indicating the *O-R* phase transitions are observed. These results show that the *O-R* phase transition in highly diluted KTN crystals can be identified by analyzing the changes of $d\nu/dT$ and I_A/I_B as a function of temperature.

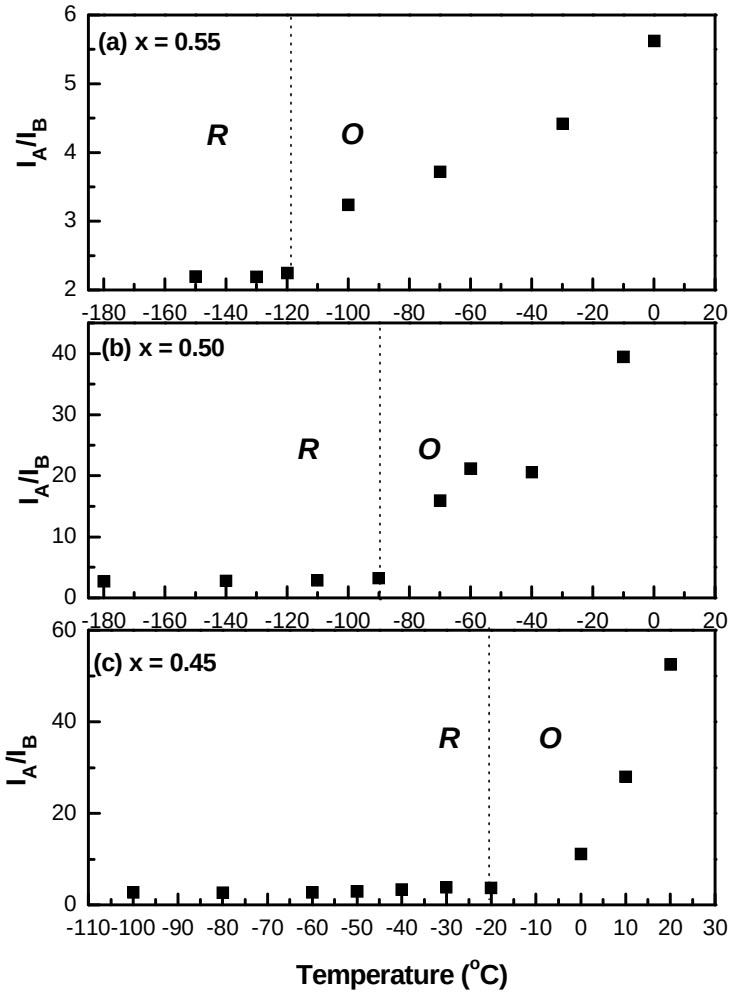

Figure 5.9. Temperature dependence of I_A/I_B for (a) $KTN_{0.55}$, (b) $KTN_{0.50}$ and (c) $KTN_{0.45}$. The dashed lines indicate the phase transition temperatures

5.4 Conclusion

In this chapter, the Raman scattering technique was used to investigate the phase transitions exhibited by highly-diluted KTN_x single crystals. The *C-T* and *T-O* phase transitions were easily identified by following the criteria used by Bartasyte *et al* [70]. The *O-R* phase transition was determined by analyzing the changes in the value of $d\nu/d$T of the modes at around 565 and 535 cm^{-1}. We also showed that the *O-R* phase transition for all

samples can be determined by the analysis of the intensity ratio I_A/I_B. The regions of existence of the phases observed are consistent with those displayed in the phase diagram determined by Triebwasser [65].

CONCLUDING REMARKS

In the present work we used several experimental techniques to investigate some of the properties of four different series of inorganic oxide crystals. The main results found are listed below.

(1) For future investigations on the defect structure of LN using neutron scattering technique, we successfully grew C^7LN crystal. We observed that the Raman modes of C^7LN are broader than those of NS^7LN, reflecting the disorder induced by the larger amount of Li vacancies on the *R3c* phase of C^7LN. This disorder also accounts for the lower values of the thermal parameters λ and κ of C^7LN as compared to those of NS^7LN and natural CLN.

(2) We investigated the changes in the phonon spectra of mixed (Nd,Yb):$Y_xGd_{1-x}(VO_4)$ crystals at room temperature. The phonon symmetry assignments were given and the observed wavenumbers were correlated with x to establish systematic variations. For Yb:$GdVO_4$, neither broadening nor wavenumber shifting of the modes were observed, indicating that Yb doping up to 0.035 produces no significant modification of the $GdVO_4$ structure. For Nd:$Y_xGd_{1-x}(VO_4)$ and *y*Yb:$Y_xGd_{1-x}(VO_4)$ we observed that the wavenumber of most of the modes increase with increasing x; irrespective of Nd and Yb levels considered.

(3) We carried out Raman measurements to determine the room temperature phonons of CBN32, KNCBN, CBN26 and NCBN crystals. We observed few and broad bands. The broadening of the bands is related to the intrinsic disorder of the TBB structure. The phonon symmetry assignments were based on correlations with previous results in other CBN and SBN compounds. We observed that the wavenumbers of the internal NbO_6 phonons increase with increasing V. This wavenumber "hardening" was associated to the decrease of the Nb-O distances when one proceeds from CBN32 to NCBN. From DSC curves we determined T_C and observed that it increases with decreasing Ca content. Temperature-dependent Raman

spectra (25-568 K) of CBN32 were recorded and the changes observed were discussed. The results indicated that CBN32 undergoes the well-known ferroelectric to paraelectric phase transition at T_C = 446 K, and a possible phase transition at 75-100 K.

(4) The phase transitions of highly-diluted KTN_x (x = 0.45, 0.50 and 0.55) single crystals have been investigated by the Raman scattering technique. The cubic to tetragonal (*C-T*) and tetragonal to orthorhombic (*T-O*) phase transitions were easily identified by following the criteria used by Bartasyte *et al* [70]. The orthorhombic to rhombohedral (*O-R*) phase transition was determined by analyzing the changes in the value of $d\nu/dT$ of the modes at around 565 and 535 cm^{-1}. We also showed that the *O-R* phase transition for all samples can be determined by the analysis of the intensity ratio I_A/I_B. The regions of existence of the phases observed are consistent with those displayed in the phase diagram determined by Triebwasser [65].

REFERENCES

［1］ Bergman, J.G., A. Ashkin, A.A. Ballman, J.M. Dziedzic, Levinste.Hj, and R.G. Smith, Applied Physics Letters, 1968. **12**(3): p. 92-&.

［2］ Carruthe.Jr, G.E. Peterson, M. Grasso, and Bridenba.Pm, Journal of Applied Physics, 1971. **42**(5): p. 1846-&.

［3］ Tomeno, I. and S. Matsumura, Journal of the Physical Society of Japan, 1987. **56**(1): p. 163-177.

［4］ Bordui, P.F., R.G. Norwood, C.D. Bird, and G.D. Calvert, Journal of Crystal Growth, 1991. **113**(1-2): p. 61-68.

［5］ Holmes, R.J. and D.M. Smyth, Journal of Applied Physics, 1984. **55**(10): p. 3531-3535.

［6］ Peterson, G.E. and Carneval.A, Journal of Chemical Physics, 1972. **56**(10): p. 4848-&.

［7］ Abrahams, S.C. and P. Marsh, Acta Crystallographica Section B-Structural Science, 1986. **42**: p. 61-68.

［8］ Lerner, P., C. Legras, and J.P. Dumas, Journal of Crystal Growth, 1968. **3-4**: p. 231-235.

［9］ Iyi, N., K. Kitamura, F. Izumi, J.K. Yamamoto, T. Hayashi, H. Asano, and S. Kimura, Journal of Solid State Chemistry, 1992. **101**(2): p. 340-352.

［10］ Wilkinson, A.P., A.K. Cheetham, and R.H. Jarman, Journal of Applied Physics, 1993. **74**(5): p. 3080-3083.

［11］ Zotov, N., H. Boysen, F. Frey, T. Metzger, and E. Born, Journal of Physics and Chemistry of Solids, 1994. **55**(2): p. 145-152.

［12］ Blumel, J., E. Born, and T. Metzger, Journal of Physics and Chemistry of Solids, 1994. **55**(7): p. 589-593.

［13］ Kojima, S., Japanese Journal of Applied Physics Part 1-Regular Papers Short Notes & Review Papers, 1993. **32**(9B): p. 4373-4376.

［14］ Repelin, Y., E. Husson, F. Bennani, and C. Proust, Journal of Physics and Chemistry of Solids, 1999. **60**(6): p. 819-825.

［15］ Wilkening, M., D. Bork, S. Indris, and P. Heitjans, Physical Chemistry Chemical Physics, 2002. **4**(14): p. 3246-3251.

［16］ Chowdhur.Mr, G.E. Peckham, R.T. Ross, and Saunders.Dh, Journal of Physics C-Solid State Physics, 1974. **7**(6): p. L99-L102.

［17］ Chowdhury, M.R., G.E. Peckham, and D.H. Saunderson, Journal of Physics C-Solid State Physics, 1978. **11**(8): p. 1671-1683.

［18］ Lighan, W.L., J.N. Hodgson, E. Cheng, and D. Dudley, CLEO 1999. p. l.

［19］ Anderson, S.G., Laser Focus World, 2001. **37**(5): p. 19-24.

［20］ Zagumennyi, A.I., et al., Sov. Journal of Quantum Electron, 1992. **22**: p. 1071-1074.

［21］ Studenikin, P.A., et al., Japan Journal of Applied Physics, 1995. **25**: p. 1162-1166.

［22］ Wyss, C.P., W. Luthy, H.P. Weber, V.I. Vlasov, Y.D. Zavartsev, P.A. Studenikin, A.I. Zagumennyi, and I.A. Shcherbakov, Applied Physics B-Lasers and Optics, 1999. **68**(4): p. 659-661.

［23］ Zhang, H.J., X.L. Meng, L. Zhu, J.H. Liu, C.Q. Wang, and Z.S. Shao, Japanese Journal of Applied Physics Part 2-Letters, 1999. **38**(11A): p. L1231-L1233.

［24］ Wang, C.Q., Y.T. Chow, L. Reekie, W.A. Gambling, H.J. Zhang, L. Zhu, and X.L. Meng, Applied Physics B-Lasers and Optics, 2000. **70**(6): p. 769-772.

［25］ Zhang, H.J., X.L. Meng, J.H. Liu, L. Zhu, C.Q. Wang, Z.S. Shao, J.Y. Wang, and Y.G. Liu, Journal of Crystal Growth, 2000. **216**(1-4): p. 367-371.

［26］ Qin, L.J., X.L. Meng, C.L. Du, Z.S. Shao, L. Zhu, B.C. Xu, and H.J. Zhang, Japanese Journal of Applied Physics Part 1-Regular Papers Short Notes & Review Papers, 2002. **41**(10): p. 6018-6019.

［27］ Zhang, H.J., J.Y. Wang, C.Q. Wang, L. Zhu, X.B. Hu, X.L. Meng, and M.H. Jiang, Optical Materials, 2003. **23**(1-2): p. 449-454.

［28］ Luo, H., D.Y. Tang, G.Q. Xie, H.J. Zhang, L.J. Qin, H.H. Yu, L.Y. Ng, and L.J. Qian, Optics Communications, 2008. **281**(21): p. 5382-5384.

［29］ Liu, J., W. Han, H. Zhang, H. Yang, and V. Petrov, Applied Physics B: Lasers and Optics, 2010. **98**(1): p. 87-91.

［30］ Zhang, H.J., J.H. Liu, J.Y. Wang, C.Q. Wang, L. Zhu, Z.S. Shao, X.L. Meng, X.B. Hu, Y.T. Chow, and M.H. Jiang, Optics and Lasers in Engineering, 2002. **38**(6): p. 527-536.

［31］ Liu, J., Y. Wan, W. Han, H. Yang, H. Zhang, and J. Wang, Applied Physics B: Lasers and Optics, 2010. **98**(1): p. 69-76.

［32］ Liu, J.H., H.J. Zhang, X. Mateos, W.J. Han, V. Petrov, and J.Y. Wang, Optics Express, 2008. **16**(22): p. 17729-17734.

［33］ Ng, S.P., D.Y. Tang, A.Q. Liu, L.J. Qin, and X.L. Meng, Optics Communications, 2006. **259**(1): p. 256-260.

［34］ He, J.L., Y.X. Fan, J. Du, Y.G. Wang, S. Liu, H.T. Wang, L.H. Zhang, and Y. Hang, Optics Letters, 2004. **29**(23): p. 2803-2805.

［35］ Liu, J.H., Z.P. Wang, X.L. Meng, Z.S. Shao, B. Ozygus, A. Ding, and H. Weber, Optics Letters, 2003. **28**(23): p. 2330-2332.

［36］ Yu, H.H., H.J. Zhang, Z.P. Wang, J.Y. Wang, Y.G. Yu, Z.S. Shao, M.H. Jiang, and X.Y. Zhang, Applied Physics Letters, 2007. **90**(23): p. -.

［37］ Nguyen, A.D., K. Murdoch, N. Edelstein, L.A. Boatner, and M.M. Abraham, Physical Review B, 1997. **56**(13): p. 7974-7987.

［38］ Harley, R.T., W. Hayes, and S.R.P. Smith, Solid State Communications, 1971. **9**(9): p. 515-&.

［39］ Guedes, I., Y. Hirano, M. Grimsditch, N. Wakabayashi, C.K. Loong, and L.A. Boatner, Journal of Applied Physics, 2001. **90**(4): p. 1843-1846.

［40］ Baran, E.J., M.E. Escobar, L.L. Fournier, and R.R. Filgueira, Zeitschrift Fur Anorganische Und Allgemeine Chemie, 1981. **472**(1): p. 193-199.

［41］ Escobar, M.E. and E.J. Baran, Zeitschrift Fur Naturforschung Section a-a Journal of Physical Sciences, 1980. **35**(10): p. 1110-1111.

［42］ Krasovec, U.O., B. Orel, A. Surca, N. Bukovec, and R. Reisfeld, Solid State Ionics, 1999. **118**(3-4): p. 195-214.

［43］ Barbero, B.P. and L.E. Cadus, Applied Catalysis a-General, 2003. **252**(1): p. 133-147.

［44］ Au, C.-T. and W.-D. Zhang, Journal of the Chemical Society, Faraday Transactions 1997. **93**(6): p. 1195-1204.

［45］ Santos, C.C., E.N. Silva, A.P. Ayala, I. Guedes, P.S. Pizani, C.K. Loong, and L.A. Boatner, Journal of Applied Physics, 2007. **101**(5): p. -.

［46］ Esser, M., M. Burianek, D. Klimm, and M. Muhlberg, Journal of Crystal Growth, 2002. **240**(1-2): p. 1-5.

［47］ Esser, M., M. Burianek, P. Held, J. Stade, S. Bulut, C. Wickleder, and M. Muhlberg, Crystal Research and Technology, 2003. **38**(6): p. 457-464.

［48］ Jamieson, P.B., S.C. Abrahams, and Bernstei.Jl, Journal of Chemical Physics, 1968. **48**(11): p. 5048-&.

［49］ Lima-Silva, J.J., I. Guedes, J. Mendes, A.P. Ayala, M.H. Lente, J.A. Eiras, and D. Garcia, Solid State Communications, 2004. **131**(2): p. 111-114.

［50］ Gao, W.L., H.J. Zhang, B.B. Huang, R.S. Wei, X.B. Hu, J.Y. Wang, M.H. Jiang, and R.I. Boughton, Physica B-Condensed Matter, 2010. **405**(16): p. 3289-3293.

［51］ Gao, W.L., H.J. Zhang, S.Q. Xia, B.B. Huang, D. Liu, J.Y. Wang, M.H. Jiang, L.M. Zheng, J.F. Wang, and C.J. Lu, Materials Research Bulletin, 2010. **45**(9): p. 1209-1212.

［52］ Song, H.L., H.J. Zhang, Q.Z. Jiang, X.G. Xu, C.J. Lu, X.B. Hu, J.Y. Wang, and M.H. Hang, Journal of Crystal Growth, 2006. **290**(2): p. 431-435.

［53］ Burianek, M., B. Joschko, I. Kerkamm, T. Schoenbeck, D. Klimm, and M. Muehlberg, Journal of Crystal Growth, 2007. **299**(2): p. 413-417.

［54］ Muehlberg, M., M. Burianek, B. Joschko, D. Klimm, A. Danilewsky, M. Gelissen, L. Bayarjargal, G.P. Gorler, and B.O. Hildmann, Journal of Crystal Growth, 2008. **310**(7-9): p. 2288-2294.

［55］ Gao, W.L., H.J. Zhang, D. Liu, M. Xu, J.Y. Wang, Y.G. Yu, M.H. Jiang, S.Q. Sun, H.R. Xia, and R.I. Boughton, Journal of Applied Physics, 2009. **105**(2): p. -.

［56］ Gao, W.L., H.J. Zhang, X. Yin, H.L. Song, J.Y. Wang, M.H. Jiang, and R.I. Boughton, Journal of Applied Physics, 2010. **107**(9): p. -.

［57］ Gao, C.Y., H.R. Xia, J.Q. Xu, C.L. Zhou, H.J. Zhang, and J.Y. Wang, Materials Letters, 2009. **63**(1): p. 139-141.

［58］ Faria, J.L.B., P.T.C. Freire, A.P. Ayala, F.E.A. Melo, J. Mendes, C.W.A. Paschoal, I.A. Santos, and J.A. Eiras, Journal of Raman Spectroscopy, 2003. **34**(10): p. 826-830.

［59］ Speghini, A., M. Bettinelli, U. Caldino, M.O. Ramirez, D. Jaque, L.E. Bausa, and J.G. Sole, Journal of Physics D-Applied Physics, 2006. **39**(23): p. 4930-4934.

［60］ Kasprowicz, D., A. Lapinski, T. Runka, A. Speghini, and M. Bettinelli, Journal of Alloys and Compounds, 2009. **478**(1-2): p. 30-33.

［61］ Kasprowicz, D., T. Runka, A. Speghini, D. Falcomer, J.G. Sole, and M. Bettinelli, Journal of Luminescence, 2008. **128**(5-6): p. 985-987.

［62］ Rytz, D., U.T. Hochli, and H. Bilz, Physical Review B, 1980. **22**(1): p. 359-364.

［63］ Sommer, D., D. Friese, W. Kleemann, and D. Rytz, Ferroelectrics, 1991. **124**(1-4): p. 231-236.

［64］ Bouziane, E. and M.D. Fontana, Journal of Physics-Condensed Matter, 1997. **9**(46): p. 10249-10260.

［65］ Triebwasser, S., Physical Review, 1959. **114**(1): p. 63-70.

［66］ Xia, H.R., L.X. Li, J.Y. Wang, Z.H. Yang, and Q.C. Guan, Chinese journal of light scattering, 1999. **11**(2): p. 81-86.

［67］ Xia, H.R., L.X. Li, J.Y. Wang, Y.G. Liu, and J.Q. Wei, Crystal Research and Technology, 2000. **35**(10): p. 1209-1214.

［68］ Svitelskiy, O. and J. Toulouse, Journal of Physics and Chemistry of Solids, 2003. **64**(4): p. 665-676.

［69］ Bouziane, E., M.D. Fontana, and M. Ayadi, Journal of Raman Spectroscopy, 2005. **36**(9): p. 872-878.

［70］ Bartasyte, A., J. Kreisel, W. Peng, and M. Guilloux-Viry, Applied Physics Letters, 2010. **96**(26): p. -.

［71］ Wohlecke, M., G. Corradi, and K. Betzler, Applied Physics B-Lasers and Optics, 1996. **63**(4): p. 323-330.

［72］ Schaufel.Rf and M.J. Weber, Physical Review, 1966. **152**(2): p. 705-&.

［73］ Lengyel, K., L. Kovacs, A. Peter, K. Polgar, and G. Corradi, Applied Physics B-Lasers and Optics, 2007. **87**(2): p. 317-322.

［74］ Ridah, A., P. Bourson, M.D. Fontana, and G. Malovichko, Journal of Physics-Condensed Matter, 1997. **9**(44): p. 9687-9693.

［75］ Zhang, D., X. Chen, Y. Jin, X. Cao, D. Zhu, Y. Wang, G. Ding, Y. Cui, C. Chen, Z. Wu, and G. Lan, Applied Physics a-Materials Science & Processing, 2001. **72**(1): p. 95-102.

［76］ Zhang, Y., Y.H. Xu, M.H. Li, and Y.Q. Zhao, Journal of Crystal Growth, 2001. **233**(3): p. 537-540.

［77］ Shi, L.H., Y.F. Kong, W.B. Yan, H.D. Liu, X.C. Li, X. Xie, D. Zhao, L. Sun, J.J. Xu, J. Sun, S.L. Chen, L. Zhang, Z.H. Huang, S.G. Liu, W.L. Zhang, and G.Y. Zhang, Solid State Communications, 2005. **135**(4): p. 251-256.

［78］ Niwa, K., Y. Furukawa, S. Takekawa, and K. Kitamura, Journal of Crystal Growth, 2000. **208**(1-4): p. 493-500.

［79］ Yao, S.H., J.Y. Wang, H. Liu, X.B. Hu, H.J. Zhang, X.F. Cheng, and Z.C. Ling, Journal of Alloys and Compounds, 2008. **455**(1-2): p. 501-505.

［80］ Choi, S.H., S. Maruyama, K.K. Kim, and J.H. Lee, Journal of the Korean Physical Society, 2003. **43**(5): p. 747-753.

［81］ Yu, Y.G., J.Y. Wang, H.J. Zhang, H.H. Yu, Z.P. Wang, M.H. Jiang, H.R. Xia, and R.I. Boughton, Journal of the Optical Society of America B-Optical Physics, 2008. **25**(6): p. 995-1001.

［82］ Qin, L.J., X.L. Meng, C.L. Du, L. Zhu, B.C. Xu, Z.S. Shao, Z.Q. Liu, Q. Fang, and R.F. Cheng, Journal of Alloys and Compounds, 2003. **354**(1-2): p. 259-262.

［83］ Qin, L.J., X.L. Meng, L. Zhu, J.H. Liu, B.C. Xu, H.Z. Xu, F.Y. Jiang, C.L. Du, X.Q. Wang, and Z.S. Shao, Chemical Physics Letters, 2003. **380**(3-4): p. 273-278.

［84］ Rousseau, D.L., R.P. Bauman, and S.P.S. Porto, Journal of Raman Spectroscopy, 1981. **10**(Jan): p. 253-290.

［85］ Kolitsch, U. and D. Holtstam, European Journal of Mineralogy, 2004. **16**(1): p. 117-126.

［86］ Isasi, J., M.L. Veiga, Y. Laureiro, R. Saezpuche, and C. Pico, Journal of Alloys and Compounds, 1991. **177**(1): p. 143-147.

［87］ Lu, G.W., C.X. Li, W.C. Wang, Z.H. Wang, H.R. Xia, and P. Zhao, Materials Science and Engineering B-Solid State Materials for Advanced Technology, 2003. **98**(2): p. 156-160.

［88］ Voron'ko, Y., A. Sobol', V. Shukshin, A. Zagumennyĭ, Y. Zavartsev, and S. Kutovoĭ, Physics of the Solid State, 2009. **51**(9): p. 1886-1893.

［89］ Moura, M.R., A.P. Ayala, I. Guedes, M. Grimsditch, C.K. Loong, and L.A. Boatner, Journal of Applied Physics, 2004. **95**(3): p. 1148-1151.

［90］ Nipko, J.C., C.K. Loong, M. Loewenhaupt, M. Braden, W. Reichardt, and L.A. Boatner, Physical Review B, 1997. **56**(18): p. 11584-11592.

［91］ Miller, S.A., H.H. Caspers, and H.E. Rast, Physical Review, 1968. **168**(3): p. 964-&.

［92］ Begun, G.M., G.W. Beall, L.A. Boatner, and W.J. Gregor, Journal of Raman Spectroscopy, 1981. **11**(4): p. 273-278.

［93］ Beall, G.W., L.A. Boatner, D.F. Mullica, and W.O. Milligan, Journal of Inorganic & Nuclear Chemistry, 1981. **43**(1): p. 101-105.

［94］ Mullica, D.F., D.A. Grossie, and L.A. Boatner, Journal of Solid State Chemistry, 1985. **58**(1): p. 71-77.

［95］ Mullica, D.F., D.A. Grossie, and L.A. Boatner, Inorganica Chimica Acta-F-Block Elements Articles and Letters, 1985. **109**(2): p. 105-110.

［96］ Mullica, D.F., W.O. Milligan, D.A. Grossie, G.W. Beall, and L.A. Boatner, Inorganica Chimica Acta-F-Block Elements Articles and Letters, 1984. **95**(4): p. 231-236.

［97］ Ni, Y.X., J.M. Hughes, and A.N. Mariano, American Mineralogist, 1995. **80**(1-2): p. 21-26.

［98］ Li, H.Y., S.Y. Zhang, S.H. Zhou, and X.Q. Cao, Inorganic Chemistry, 2009. **48**(10): p. 4542-4548.

［99］ Mullica, D.F., E.L. Sappenfield, M.M. Abraham, B.C. Chakoumakos, and L.A. Boatner, Inorganica Chimica Acta, 1996. **248**(1): p. 85-88.

［100］Lohmulle.G, G. Schmidt, B. Deppisch, V. Gramlich, and Schering.C, Acta Crystallographica Section B-Structural Science, 1973. **B 29**(Jan15): p. 141-142.

［101］Hu, X.L., J.Z. Chen, N.F. Zhuang, J.L. Chen, J.M. Lan, and F.T. Yang, Journal of Crystal Growth, 2003. **256**(3-4): p. 328-333.

［102］Burns, G., F.H. Dacol, R.R. Neurgaonkar, A.S. Bhalla, and R. Guo, Ferroelectrics, 1990. **108**: p. 189-193.

［103］Wilde, R.E., Journal of Raman Spectroscopy, 1991. **22**(6): p. 321-325.

［104］David, C., A. Tunyagi, K. Betzler, and M. Wohlecke, Physica Status Solidi B-Basic Solid State Physics, 2007. **244**(6): p. 2127-2137.

［105］Zhu, X.L., X.M. Chen, X.Q. Liu, and X.G. Li, Journal of Applied Physics, 2009. **105**(12): p. -.

［106］Xia, H.R., H.C. Chen, H. Yu, L.J. Hu, K.X. Wang, and B.Y. Zhao, Physical Review B, 1996. **54**(13): p. 8954-8957.

［107］Xia, H.R., H.C. Chen, H. Yu, K.X. Wang, and B.Y. Zhao, Physica Status Solidi B-Basic Research, 1998. **210**(1): p. 47-59.

［108］Heine, U., U. Voelker, K. Betzler, M. Burianek, and M. Muehlberg, New Journal of Physics, 2009. **11**: p. -.

［109］Cheng, J., Y. Yang, Y.H. Tong, S.B. Lu, J.Y. Sun, K. Zhu, Y.L. Liu, G.G. Siu, and Z.K. Xu, Journal of Applied Physics, 2009. **105**(5): p. -.

［110］Silberman, E., S.H. Morgan, and J.M. Springer, Journal of Raman Spectroscopy, 1981. **10**(Jan): p. 248-250.

［111］Kim, S., I.S. Yang, J.K. Lee, and K.S. Hong, Physical Review B, 2001. **6409**(9): p. -.

［112］Xu, G.Y., P.M. Gehring, and G. Shirane, Physical Review B, 2006. **74**(10): p. -.

［113］Jiang, F.M. and S. Kojima, Japanese Journal of Applied Physics Part 1-Regular Papers Short Notes & Review Papers, 1999. **38**(9A): p. 5128-5132.

［114］Wang, J.Y., X.P. Wang, Y.G. Yu, H.J. Zhang, and R.I. Boughton, Journal of Crystal Growth, 2006. **293**(2): p. 398-403.

［115］Joel W. Ager III, W. Walukiewica, M. McCluskey, M.A. Plano and M.I. Landstrass, Applied Physics Letter, 1995. **66**(5): p. 616-619.

［116］Pruvost, F., and A. Deneuville, Diamond and Related Materials, 2001. **10**: p. 531-535.

［117］Baier-Saip, J.A., E. Ramos-Moor, and A.L. Cabrera, Solid State Communications, 2005. **135**(6): p. 367-372.

［118］Trodahl, H.J., N. Klein, D. Damjanovic, N. Setter, B. Ludbrook, D. Rytz, and M. Kuball, Applied Physics Letters, 2008. **93**(26): p. -.

［119］Kuwata, J., K. Uchino, and S. Nomura, Ferroelectrics, 1981. **37**(1-4): p. 579-582.

PUBLICATIONS

[1] **Nana Zhang**, Jiyang Wang, Shuhua Yao, Xiaobo Hu, Huaijin Zhang, A. P. Ayala, I. Guedes*. "Growth and characterization of congruent lithium isotope niobate ($^{7}LiNbO_3$) single crystal". Journal of Crystal Growth. 2011 (318) 645-648 (SCI) IF: 1.737.

[2] **Nana Zhang**, Jiyang Wang, Xiaobo Hu, Huaijin Zhang, C.C. Santos, A.P. Ayala, I.Guedes*. "Phonons in isostructural (Nd, Yb):$Y_xGd_{1-x}VO_4$ laser crystals: A Raman scattering study". Journal of Solid State Chemistry. 2011 (184) 905-910 (SCI) IF: 2.261.

[3**]** **Nana Zhang**, Wenlan Gao, Huaijin Zhang, Xiaobo Xu, Jiyang Wang, C.C. Santos, A.P.Ayala, I. Guedes*, "Phonons spectra of CBN crystals." Vibrational Spectroscopy. 2012 (58) 74-78 (SCI) IF: 2.083.

[4] **Nana Zhang,** Rusheng Wei, Jiyang Wang, Xiaobo Hu, Huaijin Zhang, C.C. Santos, A.P. Ayala, I. Guedes*. "Features of orthorhombic to rhombohedral phase transitions in highly diluted KTN crystals". Journal of Alloys and Compounds. Accepted. (SCI) IF: 2.134.